



HAL
open science

Joint Inversion of Coseismic and Early Postseismic Slip to Optimize the Information Content in Geodetic Data: Application to the 2009 M w 6.3 L'Aquila Earthquake, Central Italy

Théa Ragon, Anthony Sladen, Quentin Bletery, Mathilde Vergnolle, Olivier Cavalié, Antonio Avallone, Julien Balestra, Bertrand Delouis

► To cite this version:

Théa Ragon, Anthony Sladen, Quentin Bletery, Mathilde Vergnolle, Olivier Cavalié, et al.. Joint Inversion of Coseismic and Early Postseismic Slip to Optimize the Information Content in Geodetic Data: Application to the 2009 M w 6.3 L'Aquila Earthquake, Central Italy. *Journal of Geophysical Research: Solid Earth*, 2019, 124 (10), pp.10522-10543. 10.1029/2018JB017053 . hal-02383105v1

HAL Id: hal-02383105

<https://hal.science/hal-02383105v1>

Submitted on 27 Nov 2020 (v1), last revised 3 Feb 2022 (v2)

HAL is a multi-disciplinary open access archive for the deposit and dissemination of scientific research documents, whether they are published or not. The documents may come from teaching and research institutions in France or abroad, or from public or private research centers.

L'archive ouverte pluridisciplinaire **HAL**, est destinée au dépôt et à la diffusion de documents scientifiques de niveau recherche, publiés ou non, émanant des établissements d'enseignement et de recherche français ou étrangers, des laboratoires publics ou privés.

1 **Joint inversion of co-seismic and early post-seismic slip**
2 **to optimize the information content in geodetic data:**
3 **Application to the 2009 M_w 6.3 L'Aquila earthquake,**
4 **Central Italy**

5 **Théa Ragon¹, Anthony Sladen¹, Quentin Bletery¹, Mathilde Vergnolle¹,**
6 **Olivier Cavalié¹, Antonio Avallone², Julien Balestra¹, Bertrand Delouis¹**

7 ¹Université Côte d'Azur, CNRS, IRD, Observatoire de la Côte d'Azur, Géoazur, Valbonne, France

8 ²Istituto Nazionale di Geofisica e Vulcanologia, Rome, Italy

9 **Key Points:**

- 10 • Simultaneous inversion of geodetic data with different spatio-temporal resolution
11 maximizes the information content
- 12 • If the early afterslip signal is neglected, coseismic slip is overestimated by 30% and
13 postseismic slip is underestimated by a factor of 3
- 14 • Early afterslip (6 days after mainshock) is preferentially located at the transition
15 zone between coseismic rupture and longer-term afterslip

16 **Reference:** Ragon, T., Sladen, A., Bletery, Q., Vergnolle, M., Cavali, O., Aval-
17 lone, A., et al. (2019). Joint inversion of coseismic and early postseismic slip to optimize
18 the information content in geodetic data: Application to the 2009 M_w 6.3 L'Aquila earth-
19 quake, Central Italy. *Journal of Geophysical Research: Solid Earth*, 124, 10522–10543.
20 <https://doi.org/10.1029/2018JB017053>

Corresponding author: Théa Ragon, ragon@geoazur.unice.fr

21 **Abstract**

22 When analyzing the rupture of a large earthquake, geodetic data are often critical. These
23 data are generally characterized by either a good temporal or a good spatial resolution,
24 but rarely both. As a consequence, many studies analyze the co-seismic rupture with data
25 that also include one or more days of early post-seismic deformation. Here, we invert si-
26 multaneously for the co- and post-seismic slip with the condition that the sum of the two
27 models remains compatible with data covering the two slip episodes. We validate the ben-
28 efits of this approach with a toy model and an application to the 2009 M_w 6.3 L'Aquila
29 earthquake, using a Bayesian approach and accounting for epistemic uncertainties. For
30 the L'Aquila earthquake, we find that if early post-seismic deformation is not explicitly
31 acknowledged co-seismic signal, co-seismic slip models may overestimate the peak am-
32 plitude while long-term post-seismic models may largely underestimate the total post-
33 seismic slip amplitude. This example illustrates how the proposed approach could im-
34 prove our comprehension of the seismic cycle, of fault frictional properties, and the spa-
35 tial and temporal relationship between seismic rupture, afterslip and aftershocks.

36 **1 Introduction**

37 The occurrence of earthquakes and seismic sequences is mainly controlled by the
38 spatial and temporal evolution of crustal stresses. The co-seismic stress changes and the
39 redistribution of stress following an earthquake thus both play an important role in the
40 seismic cycle and the mechanical behavior of faults, including the generation of new seis-
41 mic sequences. To understand both co-seismic and post-seismic processes, and their re-
42 lationship, is thus a crucial step to propose realistic earthquakes scenarios and reliable
43 hazard estimates.

44 While earthquakes can last for a few seconds to minutes, the subsequent period of
45 post-seismic stress relaxation can last months to years. Post-seismic relaxation is gen-
46 erally modeled by several interacting mechanisms, such as localized shear on the fault
47 (a.k.a. afterslip) [e.g. *Marone et al.*, 1991; *Freed*, 2007; *Johnson et al.*, 2012], visco-elastic
48 deformation in the lower crust or mantle [e.g. *Nur and Mavko*, 1974; *Pollitz et al.*, 1998;
49 *Freed and Burgmann*, 2004] or poroelastic rebound [e.g. *Peltzer et al.*, 1998; *Jonsson et al.*,
50 2003]. The interactions between co-seismic stress changes, aftershocks and post-seismic
51 deformation are still poorly understood [e.g. *Perfettini and Avouac*, 2007]. Slip on the
52 fault may be governed by two brittle deformation modes following rate and state fric-

53 tion laws [*Rice and L. Ruina*, 1983]: seismic rupture may occur in velocity weakening
54 areas, whereas afterslip may develop in velocity strengthening zones [e.g. *Marone et al.*,
55 1991]. In contrast, *Helmstetter and Shaw* [2009] also show that afterslip processes may
56 be primarily driven by stress heterogeneities, independently of the rate and state fric-
57 tion behavior. Aftershocks may be triggered by co-seismic stress changes, without di-
58 rect relation to post-seismic deformation [*Dieterich*, 1994]. Or, aftershocks may also be
59 primarily triggered by the post-seismic reloading due to afterslip [e.g. *Perfettini and Avouac*,
60 2004; *Hsu et al.*, 2006; *Peng and Zhao*, 2009; *Ross et al.*, 2017]. The variability of these
61 theories emphasizes the need to refine our comprehension and description of the co-seismic
62 and post-seismic phases and their transition.

63 Our understanding of the co-seismic processes mainly derives from modeling of seis-
64 mic, geodetic and tsunami data, and our understanding of post-seismic behavior is mainly
65 based on the modeling of geodetic observations [e.g. *Burgmann et al.*, 1997; *Wang et al.*,
66 2012; *Perfettini and Avouac*, 2014; *Gualandi et al.*, 2017] or simulation [e.g. *Smith and*
67 *Sandwell*, 2004; *Barbot and Fialko*, 2010; *Cubas et al.*, 2015]. Geodetic observations thus
68 remain a cornerstone to identify and characterize the co- and post-seismic processes. GNSS
69 time series are commonly used and can provide a good temporal resolution (seconds to
70 days). But the spatial resolution of such observations is usually limited, as GNSS sta-
71 tions are usually several tens or hundreds of kilometers apart. In contrast, synthetic aper-
72 ture radar interferometry (InSAR) can provide extensive spatial coverage (in the order
73 of a meter) but with a limited temporal resolution. Indeed, while earthquakes last for
74 a few seconds, very often satellites have a revisit time of more than a few days. If earth-
75 quakes do not nucleate just before the visit of a satellite, which is generally the case, the
76 measured deformation is the co-seismic signal plus a fraction of the post-seismic defor-
77 mation. As a consequence, most earthquake models based on geodetic observations are
78 biased by an unwanted post-seismic deformation signal. In practice, both co-seismic in-
79 terferograms or campaign GNSS offsets generally cover time periods extending at least
80 a few days before and after the mainshock. Pre-earthquake signals, when evidenced, are
81 usually related to small slip episodes at depth near the hypocenter [e.g. *Kato et al.*, 2012;
82 *Ruiz et al.*, 2014]. The associated surface deformation signals are usually hard to detect
83 and neglected in co-seismic studies. The post-seismic deformation happening in the first
84 few days after the mainshock is usually detectable in the geodetic data but incorporated
85 in source estimation problems as if it was part of the co-seismic signal [e.g. *Elliott et al.*,

2013; *Lin et al.*, 2013; *Cheloni et al.*, 2014; *Bletery et al.*, 2016; *He et al.*, 2017; *Salman et al.*, 2017; *Barnhart et al.*, 2018], with the justification that it is comparatively small. Similarly, post-seismic models generally do not account for observations related to the early post-seismic deformation because they are often contaminated by co-seismic signal [e.g. *D'Agostino et al.*, 2012; *Cheloni et al.*, 2014]. What we name here the early post-seismic phase corresponds to the overlooked part of the post-seismic deformation, and can last from a few hours after the mainshock in the best case, to a few days in most studies. Yet, the largest post-seismic deformation rate is expected during the first few days after the mainshock, considering that its main trend is to decrease exponentially with time after an earthquake.

This early post-seismic phase remain largely unexplored, because of the limited temporal and spatial resolution of geodetic data [e.g., *Twardzik et al.*, 2019]. Neglecting this phase may also bias our understanding of both co-seismic and post-seismic processes. And this bias is probably persisting if seismic data (i.e. purely co-seismic) are added to the inverse problem, since geodetic data tend to have a stronger control on the inferred distribution of slip, at least in the first 10 km below the Earth surface [e.g. *Delouis et al.*, 2002].

The recent advent of high-frequency GNSS has allowed the recording of the strictly co-seismic signal (10 to 30 seconds after the earthquake time occurrence) without any contamination by early post-seismic deformation [e.g., *Twardzik et al.*, 2019]. Well instrumented earthquakes are thus now characterized by at least two geodetic datasets, one being strictly co-seismic and the other which also includes some days of early after-slip. In this study, we propose a generic inversion methodology to jointly infer co-seismic and early post-seismic slip models, taking advantage of the complementary spatial and temporal resolutions of different geodetic observations (typically InSAR and image correlation data). A comparable approach has been employed by *Floyd et al.* [2016] and *Walters et al.* [2018]. To further explore the potential of the approach, we first explicitly detail the governing equations of the implementation and then evaluate the approach through a toy model. We also analyze and illustrate the benefits of the methodology with a real event, our analyses being performed in a Bayesian framework. In detail, we investigate the impact of accounting for early afterslip on co-seismic models. We consider the 2009 $M_w 6.3$ L'Aquila earthquake, Central Italy, which has been intensively studied but whose very early post-seismic phase has not been imaged. The choice of the L'Aquila event is

119 also motivated by the large density of near field observations and the overall quality of
 120 the instrumentation. Additionally, this event ruptured a relatively well known and sim-
 121 ple fault geometry, in an area where crustal properties have been investigated in detail:
 122 this will ensure the forward physics and its uncertainties can be estimated.

123 2 Inversion Framework

124 2.1 Dual time inversion of co-seismic and early post-seismic data

125 For a number of earthquakes, we have the opportunity to use two static datasets:
 126 one which is strictly co-seismic ("co") and the other which contains co-seismic and early
 127 post-seismic signal ("co+post"). To infer the strictly co-seismic and early post-seismic
 128 slip distributions, one approach could be to invert separately for the two datasets, and
 129 assume that the strictly post-seismic ("post") solution is the difference between the "co"
 130 and "co+post" models. However, in this case, the model "co" would be constrained by
 131 fewer observations (only few GNSS offsets), most of the co-seismic information being in
 132 the "co+post" dataset (dense map of InSAR offsets). An alternative approach is to as-
 133 sume that the "co+post" slip model is the sum of the "co" and "post" slip distributions
 134 [e.g., *Floyd et al.*, 2016; *Walters et al.*, 2018]. We then have:

$$\begin{cases} \mathbf{d}_{\text{co}} = \mathbf{G}_{\text{co}}^{\text{co}} \cdot \mathbf{m}_{\text{co}} \\ \mathbf{d}_{\text{co+post}} = \mathbf{G}_{\text{co+post}}^{\text{co}} \cdot \mathbf{m}_{\text{co}} + \mathbf{G}_{\text{co+post}}^{\text{post}} \cdot \mathbf{m}_{\text{post}} \end{cases} \quad (1)$$

where matrices of the Green's functions $\mathbf{G}_{\text{data}}^{\text{model}}$ have been calculated for the correspond-
 ing dataset and model. For instance, $\mathbf{G}_{\text{co+post}}^{\text{co}}$ is the matrix of the Green's functions cal-
 culated from the model "co" for the data "co+post". The Eq. 1 can also be represented
 in the following matrix form:

$$\begin{pmatrix} \mathbf{d}_{\text{co}} \\ \mathbf{d}_{\text{co+post}} \end{pmatrix} = \begin{pmatrix} \mathbf{G}_{\text{co}}^{\text{co}} & 0 \\ \mathbf{G}_{\text{co+post}}^{\text{co}} & \mathbf{G}_{\text{co+post}}^{\text{post}} \end{pmatrix} \cdot \begin{pmatrix} \mathbf{m}_{\text{co}} \\ \mathbf{m}_{\text{post}} \end{pmatrix}. \quad (2)$$

The redesigned Green's functions matrix is now composed of 3 sub-matrices. As we fo-
 cus on the early post-seismic phase, we can make the assumption that both $\mathbf{G}_{\text{co+post}}^{\text{co}}$ and
 $\mathbf{G}_{\text{co+post}}^{\text{post}}$ matrices are identical because we suppose both co-seismic and early post-seismic

deformations are elastic. We can thus write

$$\begin{pmatrix} \mathbf{d}_{\text{co}} \\ \mathbf{d}_{\text{co+post}} \end{pmatrix} = \begin{pmatrix} \mathbf{G}_{\text{co}} & 0 \\ \mathbf{G}_{\text{co+post}} & \mathbf{G}_{\text{co+post}} \end{pmatrix} \cdot \begin{pmatrix} \mathbf{m}_{\text{co}} \\ \mathbf{m}_{\text{post}} \end{pmatrix}. \quad (3)$$

If strictly post-seismic observations are available, we could also incorporate these data into our equation to help constrain the "post" model:

$$\begin{pmatrix} \mathbf{d}_{\text{co}} \\ \mathbf{d}_{\text{co+post}} \\ \mathbf{d}_{\text{post}} \end{pmatrix} = \begin{pmatrix} \mathbf{G}_{\text{co}}^{\text{co}} & 0 \\ \mathbf{G}_{\text{co+post}}^{\text{co}} & \mathbf{G}_{\text{co+post}}^{\text{post}} \\ 0 & \mathbf{G}_{\text{post}}^{\text{post}} \end{pmatrix} \cdot \begin{pmatrix} \mathbf{m}_{\text{co}} \\ \mathbf{m}_{\text{post}} \end{pmatrix}, \quad (4)$$

135 with $\mathbf{G}_{\text{post}}^{\text{post}}$ reflecting the response of the Earth for the strictly post-seismic data. The
 136 "post" dataset then corresponds to the same post-seismic time window as that covered
 137 by the "co+post" dataset.

The off-diagonal terms of the redesigned Green's function matrix allow us to make use of the "co+post" dataset to constrain both "co" and "post" models. In the following, we refer to this approach as Combined Time Windows (CTW) approach. The CTW approach can be generalized to cover various intervals of post-seismic deformation. Indeed, while for many earthquakes strictly co-seismic data are now available, non-strictly co-seismic datasets usually cover variable time intervals. If, for instance, two intervals of post-seismic deformation contaminate the co-seismic signal, with only one of these intervals observed independently, our equation 3 can be adapted as

$$\begin{pmatrix} \mathbf{d}_{\text{co}} \\ \mathbf{d}_{\text{co+post1}} \\ \mathbf{d}_{\text{co+post2}} \\ \mathbf{d}_{\text{post2}} \end{pmatrix} = \begin{pmatrix} \mathbf{G}_{\text{co}}^{\text{co}} & 0 & 0 \\ \mathbf{G}_{\text{co+post1}}^{\text{co}} & \mathbf{G}_{\text{co+post1}}^{\text{post1}} & 0 \\ \mathbf{G}_{\text{co+post2}}^{\text{co}} & \mathbf{G}_{\text{co+post2}}^{\text{post1}} & \mathbf{G}_{\text{co+post2}}^{\text{post2}} \\ 0 & 0 & \mathbf{G}_{\text{post2}}^{\text{post2}} \end{pmatrix} \cdot \begin{pmatrix} \mathbf{m}_{\text{co}} \\ \mathbf{m}_{\text{post1}} \\ \mathbf{m}_{\text{post2}} \end{pmatrix}, \quad (5)$$

138 with $\mathbf{d}_{\text{post2}}$ reflecting the surface displacement for the time interval between times 1 and
 139 2, and $\mathbf{G}_{\text{post2}}^{\text{post2}}$ and $\mathbf{m}_{\text{post2}}$ associated Green's functions and slip model. Indeed, this ap-
 140 proach could be used to investigate as many time windows of post-seismic deformation
 141 as needed.

142 To refine co-seismic models and investigate early post-seismic deformation of the
 143 L'Aquila earthquake, we follow here the approach described by Eqs 1 and 3. We do not
 144 incorporate any information on the strictly post-seismic phase to investigate the very sim-

145 ple case where only co-seismic data (contaminated or not by early post-seismic defor-
 146 mation) are available.

147 **2.2 Accounting for Epistemic Uncertainties**

148 When imaging a slip distribution on a fault, the physics of the forward model is
 149 usually assumed of minimum complexity to simplify the computation and also often be-
 150 cause we don't know well the Earth's interior rheological structure. For instance, this
 151 structure is frequently approximated as a homogenous elastic half-space and the causative
 152 fault geometry is usually reduced to a flat rectangular plane. The uncertainties related
 153 to our approximations of the physics of the Earth affect the inferred source models [*Ragon*
 154 *et al.*, 2018]. As the early post-seismic slip is of limited amplitude, it may be particu-
 155 larly impacted by uncertainties of the forward model. We thus account for epistemic un-
 156 certainties following the approach developed by *Duputel et al.* [2014] for the Earth elas-
 157 tic properties and *Ragon et al.* [2018] for the fault geometry. The epistemic uncertain-
 158 ties are calculated from the sensitivity of the Green's Functions and are included in a
 159 covariance matrix \mathbf{C}_p .

160 **2.3 Bayesian approach**

161 Our inverse problem solves for both co-seismic and early post-seismic slip param-
 162 eters, the latter being of limited amplitude. While the co-seismic parameters will be rea-
 163 sonably well constrained, multiple and probably different early post-seismic models will
 164 probably be equally realistic, as they will equally explain the observations. To get a ro-
 165 bust image of the early post-seismic phase, we thus solve our problem with a Bayesian
 166 sampling approach which relies on the AlTar package (<https://github.com/AlTarFramework/altar>),
 167 which is a rewrite of the code CATMIP [*Minson et al.*, 2013]. AlTar combines the Metropo-
 168 lis algorithm with a tempering process to realize an iterative sampling of the solution
 169 space of the source models. A large number of samples are tested in parallel at each tran-
 170 sitional step. Additionally, a resampling is performed at the end of each step to replace
 171 less probable models. The probability of each sample to be selected depends on its abil-
 172 ity to fit the observations \mathbf{d}_{obs} within the uncertainties $\mathbf{C}_x = \mathbf{C}_d + \mathbf{C}_p$, with \mathbf{C}_d the
 173 observational errors and \mathbf{C}_p the epistemic uncertainties.

174 The ability of each model parameter to solve the source problem is evaluated through
 175 repeated updates of the Probability Density Functions (PDFs)

$$f(\mathbf{m}, \beta_i) \propto p(\mathbf{m}) \cdot \exp[-\beta_i \cdot \chi(\mathbf{m})], \quad (6)$$

where \mathbf{m} is the current sample, $p(\mathbf{m})$ is the prior information on this sample, i corresponds to each iteration and β evolves dynamically from 0 to 1 to ensure an exhaustive exploration of the solution space [Minson *et al.*, 2013]. $\chi(\mathbf{m})$ is the misfit function:

$$\chi(\mathbf{m}) = \frac{1}{2}[\mathbf{d}_{\text{obs}} - \mathbf{G} \cdot \mathbf{m}]^T \cdot \mathbf{C}_\chi^{-1} \cdot [\mathbf{d}_{\text{obs}} - \mathbf{G} \cdot \mathbf{m}]. \quad (7)$$

176 The use of AlTar with the CTW approach allows us to specify prior information on each
 177 model, and thus to ensure the quasi-positivity of both co-seismic and post-seismic slip
 178 models (or of any time window model).

179 The impact of different approaches to regularization, along with the ad-hoc choice
 180 of smoothing parameters, may bias or induce unwanted artefacts in inferred slip mod-
 181 els [e.g., Du *et al.*, 1992; Beresnev, 2003; Aster *et al.*, 2005; Causse *et al.*, 2010; Gallovic
 182 *et al.*, 2015; Gombert *et al.*, 2017]. Because our Bayesian approach aims at sampling all
 183 possible families of models compatible with the observations, it doesn't include any ad-
 184 hoc regularization parameter [e.g., Minson *et al.*, 2013].

185 **3 Application to a simplified 2D model**

186 To ensure that our methodology allows us to reliably infer the slip distribution of
 187 different time windows, we first analyze a synthetic 2D case where the slip is imaged ei-
 188 ther independently or with the CTW approach. For this case, we assume two time win-
 189 dows named co-seismic and post-seismic for simplicity.

190 **3.1 Forward Model**

191 We assume a fault extending infinitely along strike and which is 20 km wide along
 192 dip. The fault is discretized along dip into sub-faults of 1 km width and is dipping 55° .
 193 We assume the co-seismic slip on this fault to be purely dip-slip and to vary gradually
 194 with depth between 0 m and 1.5 m, positive values indicating normal slip, with maxi-
 195 mum slip between 9 and 14 km depth. We also assume that there is post-seismic slip on
 196 the same fault, with a similar location and direction and an amplitude equal to a tenth

197 of the co-seismic slip amplitude. We compute the corresponding "co" and "co+post" syn-
 198 thetic observations using the expressions of surface displacement in an homogeneous elas-
 199 tic half-space [Segall, 2010]. These synthetic observations are computed for a profile line
 200 of 100 points, centred on the fault at the surface and spaced every kilometer. The toy
 201 model and synthetic data setup are illustrated in Figure S1. For each data point, the syn-
 202 thetic observations describe the surface displacement along the profile line and the ver-
 203 tical (the along strike displacement being null). A correlated Gaussian noise of 5 mm
 204 (i.e., noise with a Gaussian amplitude distribution with 5 mm of standard deviation, char-
 205 acterized by an exponential covariance) is added to the synthetic data to simulate mea-
 206 surement errors. Note that, for this toy model, the number of "co" data is the same as
 207 the number of "co+post" observations.

208 Using these 100 synthetic observation points, we then estimate the depth distri-
 209 bution of slip still assuming a homogeneous elastic half-space. We use a uniform prior
 210 distribution $p(\mathbf{m}) = \mathcal{U}(-1 \text{ m}, 5 \text{ m})$ for the dip slip component (uniform implies that all
 211 values are considered equally likely with no a priori knowledge), a zero-mean Gaussian
 212 prior $p(\mathbf{m}) = \mathcal{N}(-0.1 \text{ m}, 0.1 \text{ m})$ on the strike-slip component and include 5 mm of ob-
 213 servational uncertainty in \mathbf{C}_d . We do not account for epistemic uncertainties as our for-
 214 ward model is identical to the one used to generate the data. We first solve for the "co"
 215 and "post" slip following the CTW approach (Figures 1a and 1c). Then, we run inde-
 216 pendent inversions, one to solve for the "co" slip (Figure 1b) and the other one to in-
 217 fer the "co+post" slip. We calculate the post-seismic solution as the difference between
 218 the "co" and "co+post" models (Figure 1d).

219 3.2 Results

220 Both independent and CTW inversion approaches allow to correctly infer the "co"
 221 slip, as the median of the PDFs is very close to the target model (Figures 1a and 1b).
 222 As expected from the inversion of surface data, the resolution is very good on shallow
 223 parts of the fault but quickly decreases with depth. The posterior uncertainty on the deep-
 224 est parameters is slightly decreased in both approaches because the lower tip of the fault
 225 acts as an additional constraint. In contrast, the inversion methodology has a larger im-
 226 pact on the inferred "post" slip distributions. When jointly inverting "co" and "co+post"
 227 observations, the true "post" slip is estimated accurately for almost all subfaults (Fig-
 228 ure 1c). When solving the two slip stages separately, the mean of the models is not as

229 good at estimating the target model (Figure 1d). The reduced posterior uncertainty of
 230 the "post" model for the independent inversion is an artifact resulting from the subtrac-
 231 tion of two gaussian-shaped curves.

232 In summary, both of the inversion approaches allow to reliably infer the "co" slip
 233 distributions, probably because its signal is dominating in the observations. But the CTW
 234 approach provides a more robust estimation of the "post" slip distribution. In this 2D
 235 case, co-seismic and co+post signals have been observed by the same number of stations.
 236 However, for most earthquakes, the number of "co" data points available (usually GNSS)
 237 will be very limited compared to the quantity of "co+post" observations (usually InSAR).
 238 We thus expect that if performing independent inversions for a real event, the inferred
 239 "co" slip distribution will be less reliable than in the case of a CTW inversion, where the
 240 whole "co+post" dataset is used to guide the choice of co-seismic parameters. We now
 241 compare these two approaches on a real earthquake.

242 **4 Application to the 2009 M_w 6.3 L'Aquila earthquake, Central Italy**

243 The L'Aquila earthquake nucleated within the Apennines orogenic system (Figure 2),
 244 where the current seismic activity results from the ongoing extensional tectonics of the
 245 area. The mainshock nucleated on the Paganica fault [Figure 2, *Atzori et al.*, 2009; *Fal-*
 246 *cucci et al.*, 2009; *Chiaraluce et al.*, 2011; *Vittori et al.*, 2011; *Lavecchia et al.*, 2012; *Ch-*
 247 *eloni et al.*, 2014], southwest of the city of L'Aquila, and has been followed by at least
 248 4 aftershocks of $M_w > 5$ [*Scognamiglio et al.*, 2009; *Chiarabba et al.*, 2009; *Pondrelli et al.*,
 249 2010]. Although the L'Aquila earthquake has been intensively studied, most co- and post-
 250 seismic models have considered the first days of post-seismic deformation as if they were
 251 part of the co-seismic phase [e.g. *Anzidei et al.*, 2009; *Atzori et al.*, 2009; *Cheloni et al.*,
 252 2010; *Trasatti et al.*, 2011; *Cirella et al.*, 2012; *D'Agostino et al.*, 2012; *Cheloni et al.*,
 253 2014; *Balestra and Delouis*, 2015; *Volpe et al.*, 2015]. To avoid the contamination of co-
 254 seismic signal by early afterslip, *Yano et al.* [2014] proposed to explore independently
 255 the early post-seismic deformation, yet with datasets covering different time intervals (1
 256 day after the mainshock for GNSS, 6 days for InSAR). Significant post-seismic displace-
 257 ment is recorded up to several months after the mainshock [e.g. *D'Agostino et al.*, 2012;
 258 *Gualandi et al.*, 2014; *Cheloni et al.*, 2014; *Albano et al.*, 2015], yet most studies of long-
 259 term post-seismic signal did not analyze the first few days of post-seismic deformation.

260 4.1 Data, Forward Model and Prior Information

261 From a geodetic perspective, this event has been particularly well documented. We
 262 can distinguish two main static datasets: one which is strictly co-seismic ("co", using con-
 263 tinuous GNSS data), and the other which also includes several days of post-seismic slip
 264 ("co+post", using cGNSS and InSAR). Two SAR images were acquired 6 days after the
 265 mainshock rupture, making the L'Aquila earthquake a perfect case study for our pro-
 266 posed approach. The "co" dataset corresponds to surface displacements measured be-
 267 tween the earthquake time occurrence (t_0) and 25-30 s after t_0 , and includes the static
 268 offsets of 41 (including high-rates) GPS stations surrounding the earthquake area pro-
 269 cessed by *Avallone et al.* [2011]. The "co+post" dataset covers the co-seismic phase plus
 270 6 days of post-seismic slip, documented by 40 static GPS offsets and 2 InSAR frames:
 271 an ascending COSMO-SkyMed frame and a descending Envisat frame (Tab. S1). The
 272 observations and their processing are detailed in Supplementary Material [Section S1,
 273 *Rosen et al.*, 2004; *Lohman and Simons*, 2005; *Jolivet et al.*, 2012].

274 The Paganica fault is generally thought to be responsible for the co-seismic rup-
 275 ture of the L'Aquila earthquake, and also for most of its post-seismic deformation [*D'Agostino*
 276 *et al.*, 2012; *Cheloni et al.*, 2014; *Yano et al.*, 2014] along with the northernmost Cam-
 277 potosto fault [Figure 2, *Gualandi et al.*, 2014]. Although the distribution of relocalized
 278 aftershocks and surface rupture suggest that the Paganica fault system is possibly seg-
 279 mented [*Boncio et al.*, 2010; *Lavecchia et al.*, 2012] and/or curved at depth [*Chiaraluce*
 280 *et al.*, 2011; *Lavecchia et al.*, 2012; *Valoroso et al.*, 2013], its geometry remains poorly
 281 constrained below the surface. The variability of published morphologies for the causative
 282 fault [*Lavecchia et al.*, 2012] suggests that even with a large amount of observations and
 283 a great seismotectonic knowledge of the area, it is not possible to determine a unique fault
 284 geometry. This is why we approximate the Paganica fault geometry as a planar surface.
 285 We determine strike and position from the trace of the co-seismic surface rupture [*EMER-*
 286 *GEO Working Group*, 2010; *Boncio et al.*, 2010] and formerly identified seismogenic faults
 287 [e.g. *Boncio et al.*, 2004b]. We select the dip and width based on aftershock relocations
 288 and focal mechanisms [e.g. *Chiaraluce et al.*, 2011; *Chiaraluce*, 2012; *Valoroso et al.*, 2013].
 289 Hence, our preferred geometry extends over 25 km south of coordinates (13.386° E, 42.445°
 290 N) with a strike of $N142^\circ$. We set fault dip at 54° and width at 18 km, such that the
 291 fault is reaching the ground surface. This geometry is in agreement with already pro-
 292 posed causative structures [e.g. *Lavecchia et al.*, 2012]. The fault is divided into 154 sub-

293 faults of 1.8 km length and 1.6 km width. As our fault geometry does not reflect the re-
 294 ality and is poorly constrained, we account for its uncertainties [*Ragon et al.*, 2018, 2019]
 295 and assume a standard deviation on the fault dip of 5° and on the fault position (the
 296 fault position varying perpendicularly from the fault trace) of 1.5 km, regarding the dis-
 297 crepancies between published fault models [e.g. *Lavecchia et al.*, 2012]. We do not ac-
 298 count for uncertainties in the fault strike for simplicity, and because its influence might
 299 be small when uncertainty in the fault position is already acknowledged [*Ragon et al.*,
 300 2019].

301 We perform the static slip inversion assuming a 1-D layered elastic structure de-
 302 rived from the CIA velocity model [*Herrmann et al.*, 2011], and calculate Green’s func-
 303 tions with the EDKS software [*Zhu and Rivera*, 2002]. We precompute Green’s functions
 304 at depths intervals of 500 m down to 15 km depth and every 5 km below. Laterally, the
 305 Green’s functions are computed every kilometer to reach the maximum epicentral dis-
 306 tance of 100 km. Then, we interpolate and sum pre-computed Green’s functions given
 307 our fault geometry and data locations. The strong variability in published elastic mod-
 308 els for the central Italy [*Herrmann et al.*, 2011] can have a strong influence on co-seismic
 309 slip estimates [e.g. *Trasatti et al.*, 2011; *Volpe et al.*, 2012; *Gallovic et al.*, 2015]. We thus
 310 account for the uncertainties in our Earth model [*Duputel et al.*, 2014] assuming a stan-
 311 dard deviation on shear modulus of 4 % at depths greater than 15 km and 13 % above.
 312 These values have been chosen a priori considering the variability between layered mod-
 313 els and the horizontal variability of 3D crustal models for several depth intervals [*Magnoni*
 314 *et al.*, 2014].

315 We perform our static slip inversion as previously detailed in Section 2. We spec-
 316 ify prior distributions for each model parameter: a zero-mean Gaussian prior $p(\mathbf{m}) =$
 317 $\mathcal{N}(-10 \text{ cm}, 10 \text{ cm})$ on the strike-slip component (we assume that, on average, the slip di-
 318 rection is along dip) and we consider each possible value of dip-slip displacement equally
 319 likely if it does not exceed 20 cm of reverse slip and 5 m of normal slip: $p(\mathbf{m}) = \mathcal{U}(-$
 320 $20 \text{ cm}, 500 \text{ cm})$.

321 4.2 Co-seismic and early post-seismic slip models

322 We will start by analyzing models inferred by the independent approach as applied
 323 to the two datasets. The first model is inferred from "co" data (model COgps) and the

324 second is estimated from the "co+post" dataset (model COPOST). The "co+post" dataset
325 is similar to what has been used in several previous studies to infer the co-seismic slip
326 [*Cirella et al.*, 2012; *D'Agostino et al.*, 2012; *Cheloni et al.*, 2014; *Yano et al.*, 2014; *Volpe*
327 *et al.*, 2015]. The results of these two inversions will then be compared to those of the
328 CTW inversion. For the sake of comparison, these inversions are performed without ac-
329 counting for epistemic uncertainties. This refinement will only be added in a final inver-
330 sion.

331 For each approach, we estimate 300,000 samples among the most plausible mod-
332 els of the full solution space. This set of samples provides information on the possible
333 parameter values and on their uncertainty. Mean and median models are basic proba-
334 bilistic values but can give a good overview of the range of most likely solutions. More
335 detailed quantities, such as the marginal posterior distribution of a given parameter or
336 the variability of slip between neighbor subfaults, will inform on the uncertainty and trade-
337 off of the inversion. Yet, the mere interpretation of average and median samples should
338 be taken with caution: the mean model does not reflect the uncertainty of inferred pa-
339 rameters, and it does not reproduce either the covariance between several parameters.

340 As we are tied to the need of presenting our results with 2D figures when the ex-
341 ploration is done on a parameter space with tenth of dimensions, we choose to represent
342 our results in 3 different ways. For the first representation (e.g., Figures 3a-d, 5a-b), we
343 divide our set of 300,000 samples into 25 families, and represent the median model of each
344 family as subdivisions of subfaults (each subfault is thus divided in 25 pixels, more in-
345 formation in Figure S3). The first family gathers samples with parameters of less than
346 50 cm offset from the mean model parameters. Other families are built iteratively around
347 a randomly selected model that has not fitted within antecedent families, except for the
348 last family which regroups orphan samples). This first representation illustrates the vari-
349 ability in slip amplitude for a particular parameter. Also, it allows for a visual estima-
350 tion of the covariance between neighbor parameters: if samples that infer large dip-slip
351 on a subfault infer small dip-slip on its neighbor subfault, and vice versa, then there is
352 a trade-off between these two parameters.

353 A second representation shows the posterior marginal Probability Density Func-
354 tions of the dip-slip parameters which, for a particular parameter, will inform on the amount
355 of slip uncertainty associated to each subfault (e.g. Figures 3e-g, 5c-e). In particular, the

356 shape and width of the posterior PDF can be considered as a proxy of the model res-
 357 olution for the inferred parameter.

358 The third representation is a classic map view of the dip-slip amplitude and rake
 359 of the mean model (e.g. Figures a and b in S4, S8, S12).

360 **4.2.1 Approaches assuming independent datasets**

361 When solving for the model COgps, we find that most of the slip is concentrated
 362 in the shallow parts of the fault (Figures 3a, S4a,c,e). Slip amplitudes reach 230 cm in
 363 the first two kilometers below the Earth surface. These values largely contradict field
 364 observations hardly reporting more than 15 cm of surface offset [*Faluccci et al.*, 2009;
 365 *Vittori et al.*, 2011]. This contradiction probably derives from our limited set of obser-
 366 vations, with only 4 GPS stations documenting the rupture in the near field (Figure 4a).
 367 The COgps model is thus largely under-determined and unlikely to represent a reliable
 368 image of the co-seismic deformation. In contrast, the COPOST slip model is inferred from
 369 a more populated dataset extending over a large part of the Paganica fault (Fig. 3b, S4b).
 370 The patch of highest slip amplitude, reaching more than 150 cm, is well constrained and
 371 located between 5 to 7 km depth (Figure 3b). Up to 100 cm slip is also inferred below
 372 the hypocenter. The inferred slip is almost purely dip-slip (Fig. S4b,d,f). The scalar seis-
 373 mic moment of model COPOST, calculated with $\mu = 3.5 \cdot 10^{10}$, is $M_0 = 4.9 \pm 0.67 \cdot 10^{25}$
 374 dyne.m. This value corresponds to a M_w 6.4 earthquake rather than a M_w 6.3.

375 The comparison between observations and predicted surface displacement is shown
 376 in Figure 4 for the GPS datasets and in Figure S5 for the interferograms. As expected,
 377 the COgps model well explains the "co" dataset (Figure 4b), but its predictions hardly
 378 fit the interferograms of the "co+post" dataset (Table S2). In contrast, the predicted
 379 surface displacement of the COPOST model well approaches the "co+post" observations
 380 (Figures 4b and S5), with limited residuals (Tab. S2). The surface displacement that hap-
 381 pened up to 6 days after the mainshock is similar when estimated with GPS or with the
 382 ENVISAT interferogram (Figure S6). Yet, the displacement measured with the COSMO-
 383 SkyMed interferogram differs from the one measured with GPS, particularly for the high-
 384 rate GPS station CADO (Figure S7). This misfit could be related to unwrapping errors
 385 or effects that has not been completely corrected, explaining why the COSMO-SkyMed
 386 data are systematically less well fitted by predictions than other observations.

387 **4.2.2 Dual time approach, without epistemic uncertainties**

388 With the CTW approach, we infer two slip models: the strictly co-seismic model
 389 sCO (see Figures 3c, S8a,c,e and S9 for an animated compilation of probable models)
 390 and the model sPOST which reflects the 6 days displacement following the mainshock
 391 (Figures 3d and S8b,d,f). The model sCO, exploiting information from both the "co"
 392 and "co+post" datasets, is in agreement with the main characteristics of the COPOST
 393 model (Figure 3b): the location, rake and amplitude of the maximum slip patch are com-
 394 parable (Figures S8a,c,e), and a large amount of slip is also inferred at depth, up to 75
 395 cm on average and exceeding 150 cm for some models (Figure 3c). However, unlike the
 396 COPOST model, the two main slip patches of the sCO model are delimited by an un-
 397 ruptured area (Figure 3c). Overall, the two models differ on average by 44% and by up
 398 to 75% for some subfaults characterized by high slip amplitudes (Figures 3e-g, S10), mainly
 399 because of the variability of the amount of slip inferred below 5 km depth. For the model
 400 sCO, $M_0 = 3.50 \pm 0.63 \cdot 10^{20}$ N.m and is equivalent to a moment magnitude of 6.3, cor-
 401 responding to the GCMT value of 6.3.

402 With the CTW approach, we also find that a large portion of the fault slipped dur-
 403 ing a 6 days time window after the mainshock (Figure 3d), with maximum amplitude
 404 of 30 cm in the dip-slip direction (Figure S8b). The largest post-seismic slip (≈ 45 cm)
 405 is located between the co-seismically ruptured patches (Figure 3c), and is well constrained
 406 with only 15 cm of posterior uncertainty (Figure S8f). Overall, post-seismic slip (30 cm
 407 and below) tends to locate around the highest co-seismic slip patch and the hypocen-
 408 ter, but also overlaps the deepest co-seismic slip patch. Yet, below 10 km depth, the pos-
 409 terior uncertainty can reach 100% of the median slip amplitude, meaning that the res-
 410 olution is poor and that it is difficult to interpret anything at that level of detail (Fig-
 411 ures S8d,f). The seismic moment of model sPOST is $M_0 = 1.58 \pm 0.63 \cdot 10^{20}$ N.m. The
 412 predicted surface displacements fit well the observations (Figures 4c,d and Figure S11)
 413 with residuals similar to the ones of the COPOST model (Tab. S2).

414 As expected, the areas of largest post-seismic slip in the sPOST model correspond
 415 to the locations of largest divergence between COPOST and sCO models (3b-g). In sum-
 416 mary, usual approaches using independent datasets do not allow us to infer reliable im-
 417 ages of the strictly co-seismic and early post-seismic phases. Whereas the "co+post" slip
 418 model is reliable, the "co" model is not robust enough to retrieve the early afterslip from

419 the subtraction of these two slip distributions. Additionally, the scalar seismic moment
 420 of model "co+post" corresponds to a moment magnitude greater than the GCMT M_w
 421 of 6.3. In contrast, the CTW approach allows us to infer robust estimates of both co-
 422 seismic and post-seismic slip, to exploit all the information collected within our geode-
 423 tic observations, and to correctly estimate the seismic moment. However, the reliabil-
 424 ity of these models can be questioned as they do not account for uncertainties in the for-
 425 ward model.

426 ***4.2.3 Dual time approach, accounting for epistemic uncertainties***

427 Here, we present the results of the CTW approach, as in the previous section, but
 428 accounting for epistemic uncertainties. We will name the resulting models COpref and
 429 POSTpref since they correspond to our preferred approach providing the most complete
 430 and objective evaluation of the problem (see Figures 5, 6, S12 and S14 for an animated
 431 compilation of probable co-seismic models). The distribution of the co-seismic slip dif-
 432 fers by 42% on average and by up to 88% locally from the models inferred without ac-
 433 counting for uncertainties (Figures 5c, S13). The co-seismic slip is now limited (on av-
 434 erage) to a single 10 km long patch located between 5 and 10 km depth, reaching more
 435 than 150 cm amplitude to the south (right-hand side of Figure 5a), with a rake of 90°
 436 that does not vary along the patch (left-hand side of Fig. 6). The corresponding scalar
 437 seismic moment $M_0 = 3.03 \pm 0.64 \cdot 10^{20}$ N.m is slightly lower than what was estimated
 438 for the model sCO but is still very close ($M_w = 6.28 \pm 0.06$) to the (GCMT) value of
 439 M_w 6.3.

440 Compared to the COpref model, the main characteristics of the POSTpref model
 441 are not strongly affected by the inclusion of uncertainties. Overall, post-seismic slip (20
 442 cm and below) occurs mostly below the co-seismic high slip patch, where almost no (less
 443 than 20 cm) co-seismic slip is imaged. Subfaults with the largest post-seismic slip (more
 444 than 40 cm, almost purely dip-slip as shown in the right-hand side of Fig. 6) tend to be
 445 located around or on the edges of the co-seismic high slip patch (Figure 5b). The pres-
 446 ence of large post-seismic slip below 10 km depth is unlikely as the posterior uncertainty
 447 reaches 150% of the median slip (the resolution is poor at depth, Figure S12). Thus, only
 448 3 narrow zones most probably slipped post-seismically (see Figure 5b, and a compari-
 449 son of median and maximum a posteriori models in Figure S15). M_0 is similar to model
 450 sPOST with a value of $1.60 \pm 0.63 \cdot 10^{20}$ N.m. The addition of epistemic uncertainties

451 has increased the residuals between observations and predictions (see Tab. S2 and Fig-
 452 ure S16). This behavior was expected as the inclusion of C_p allows the inversion to tol-
 453 erate for larger misfits at data points where the forward model predictions are less re-
 454 liable [Ragon *et al.*, 2018, 2019].

455 In summary, the CTW approach shows that if early post-seismic is not acknowl-
 456 edged as post-seismic signal, co-seismic models may be biased by more than 40% on av-
 457 erage and of up to 75% locally. But we also learn from these different tests that adding
 458 more data into the problem is not sufficient, and epistemic uncertainties remain criti-
 459 cal for the inference of a reliable model. Altogether, our results emphasize the need to
 460 account for two types of bias in the slip models: the contamination of co-seismic obser-
 461 vations by some early post-seismic signal, and not acknowledging the uncertainties as-
 462 sociated with the forward problem.

463 5 Discussion

464 5.1 Discussion of the CTW approach

465 Observations of co-seismic or post-seismic processes are often contaminated by other
 466 sources of deformation (mainly post-seismic or co-seismic, respectively) and are widely
 467 used, as non-contaminated data are rare and scarcely distributed. Optimizing the use
 468 of the information content in each dataset is thus critical to improve the robustness of
 469 both co-seismic and post-seismic slip models. A first approach would be to account for
 470 potential uncertainties in the co-seismic model due to early afterslip in the form of a co-
 471 variance matrix, as already proposed in *Bletery et al.* [2016]. While this approach helps
 472 inferring more reliable co-seismic models at a low computational cost, it does not allow
 473 us to estimate the early afterslip and needs a prior evaluation of the amount of afterslip
 474 considered as co-seismic signal. Another strategy would be to jointly infer "co" and "co+post"
 475 data as if they were strictly co-seismic, and to select models that better explain the "co"
 476 observations, as in [Chlieh *et al.*, 2007]. In this case, the computational cost is increased
 477 because several models have to be tested. Additionally, with these approaches the early
 478 post-seismic slip is not estimated. In contrast, the CTW approach we use in this study
 479 allows us to discriminate co-seismic from early post-seismic slip and to reliably estimate
 480 corresponding slip models, as suggested also by the results of *Floyd et al.* [2016] and *Wal-*
 481 *ters et al.* [2018]. The CTW approach takes advantage of the InSAR data that recorded

482 both co- and post-seismic deformation to help constrain both strictly co- and early post-
483 seismic models.

484 Our results on the L'Aquila event show that the early afterslip, here correspond-
485 ing to 6 days after the co-seismic rupture, can reach a fourth to a third of the amplitude
486 of the co-seismic slip. If the early afterslip is acknowledged as co-seismic signal, co-seismic
487 models of the L'Aquila event are biased. The impact of early afterslip on the co-seismic
488 models is particularly large in the case of the L'Aquila event and questions the generic
489 nature of this result. Overall, early afterslip remains poorly studied but has been shown
490 to range from 0.6% to more than 8% of the co-seismic peak slip in the first 3-4 hours fol-
491 lowing an earthquake [respectively for the 2009 great Tohoku-Oki earthquake and the
492 2012 M_w 7.6 Nicoya earthquake, *Munekane, 2012; Malservisi et al., 2015*]. *Twardzik et al.*
493 [2019] also conclude that co-seismic models may be biased by more than 10 % if the early
494 post-seismic deformation is neglected. Thus, that the post-seismic deformation ongoing
495 6 days after the mainshock reaches up to 20 % of the co-seismic slip of the L'Aquila earth-
496 quake might not be an extreme case.

497 Our tests also demonstrate that models are largely impacted by the introduction
498 of epistemic uncertainties (Figure 7). This impact could mean the assumed fault and Earth
499 properties are not realistic enough to capture the real seismic rupture, and/or that small
500 variations of the fault geometry (slight curvature, roughness) or of the Earth model (3D
501 heterogeneities) largely affect our slip models. The influence of epistemic uncertainties
502 is greater on the co-seismic model, as expected from the fact that these uncertainties scale
503 with the amount of slip [*Duputel et al., 2014; Ragon et al., 2018*]. Accounting for uncer-
504 tainties of the forward model allowed us to exclude the possibility of deep slip for the
505 co-seismic models, but not totally for the post-seismic models probably because of the
506 much lower slip amplitudes. Additionally, accounting for C_p prevented the most prob-
507 able co- and post-seismic slips to overlap in deeper parts of the fault. The inclusion of
508 epistemic uncertainties acts like a smoothing constraint on the slip distribution, but with
509 a smoothing factor being controlled by the inaccuracies of the forward problem.

510 **5.2 Non-uniqueness of co-seismic and afterslip models of the L'Aquila**
 511 **earthquake**

512 Our results on the L'Aquila event indicate that the strictly co-seismic slip is con-
 513 centrated in a thin horizontal band located between 5 and 7 km depth and reaching more
 514 than 150 cm in amplitude at its southern end, with no large slip amplitudes inferred be-
 515 low 8 km depth (Figures 6 and 8). The highest amplitude is reached at about 6 km depth
 516 south west of the hypocenter, a rupture area also imaged in the co-seismic models of *Gua-*
 517 *landi et al.* [2014], *Gallovic et al.* [2015] and *Cirella et al.* [2012] (inferred respectively
 518 from GPS only, from accelerometric and high rate GPS data, and from GPS, InSAR and
 519 strong motion, see Figure 8) and most of other authors [*Atzori et al.*, 2009; *Trasatti et al.*,
 520 2011; *D'Agostino et al.*, 2012; *Serpelloni et al.*, 2012; *Cheloni et al.*, 2014; *Balestra and*
 521 *Delouis*, 2015; *Volpe et al.*, 2015]. It is the only recurrent pattern we can notice between
 522 the 4 slip models of Figure 8. Indeed, while we do not image any shallow slip, other pub-
 523 lished slip models do with up to 1.5 m in amplitude [Figure 8, *Cirella et al.*, 2012; *Volpe*
 524 *et al.*, 2015]. Our results suggest that this imaged shallow co-seismic slip may rather be
 525 early post-seismic slip (Figure 8). At greater depths, most authors infer large slip am-
 526 plitudes while our preferred model shows no slip below 8 km depth.

527 The imaged patches of post-seismic slip (≥ 15 cm) are located around our co-seismic
 528 slip, near its hypocenter and southern end. Interestingly, our inferred post-seismic slip
 529 is also located near areas that ruptured co-seismically as inferred by other studies (Fig-
 530 ure 8). The post-seismic slip that occurred several days to months after the mainshock
 531 is characterized by 3 wide slip areas, located SW of the main co-seismic slip patch, above
 532 the hypocenter close to the surface, and around the hypocenter [*D'Agostino et al.*, 2012;
 533 *Cheloni et al.*, 2014; *Gualandi et al.*, 2014]. Most of these post-seismic models incorrectly
 534 treat the first days of post-seismic signal as a co-seismic deformation. While we infer likely
 535 afterslip in similar locations, the afterslip patches are limited to narrower areas near the
 536 co-seismic rupture (Figure 9). Most of these longer-term post-seismic models cover time
 537 periods ranging from 6 days to 9 months after the mainshock, they overlook a large part
 538 of the early post-seismic deformation. Thus, the peak amplitude of the early afterslip
 539 is up to 3 times larger than what was imaged for several months by *D'Agostino et al.*
 540 [2012] and *Cheloni et al.* [2014].

541 Our results show that the amplitude and distribution of long-term afterslip may
 542 be largely underestimated (here by a factor of 3) if the deformation occurring the first
 543 few hours to days after the mainshock is not accounted in the post-seismic budget. Thus,
 544 overlooking the early part of the postseismic phase measured in geodetic data may not
 545 only bias the estimates of the coseismic slip, but also our estimates of the postseismic
 546 phase.

547 **5.3 Fault frictional properties and relationship between afterslip and af-** 548 **tershocks**

549 The comparison between our early post-seismic model and images of longer-term
 550 post-seismic slip suggest that afterslip may nucleate preferentially around the co-seismic
 551 rupture in the days following the mainshock (Figure 9b). Afterwards, the afterslip prop-
 552 agates and extends, both along-dip and laterally, away from the co-seismic slip [*D'Agostino*
 553 *et al.*, 2012; *Cheloni et al.*, 2014; *Gualandi et al.*, 2014]. This behavior agrees with mod-
 554 els explaining afterslip as a result of rate dependent friction behavior. Indeed, in these
 555 models the afterslip relaxes the stress increment induced in velocity-strengthening area
 556 by the co-seismic rupture [*Marone et al.*, 1991; *Perfettini and Avouac*, 2004]. The post-
 557 seismic sliding thus nucleates close to the mainshock asperity and propagates with time
 558 outward from the rupture zone. That early afterslip relates to the stress changes induced
 559 by the co-seismic rupture has also been modeled for other events [e.g. the M_w 8.0 Tokachi-
 560 oki, M_w 7.6 Chi-Chi, and the M_w 6.0 Parkfield, *Miyazaki et al.*, 2004; *Chan and Stein*, 2009;
 561 *Wang et al.*, 2012, respectively].

562 Additionally, our results show that early afterslip nucleates within narrow areas (1-
 563 2 km wide), and does not happen everywhere around the co-seismic rupture. Areas slid-
 564 ing aseismically just after the mainshock are thus limited in size around the co-seismic
 565 rupture, suggesting that frictional properties vary at a small-scale around the rupture
 566 zone. It may also suggest that the regions adjacent to co-seismic rupture are potentially
 567 unstable (i.e. are steady-state velocity weakening). This interpretation agrees with the
 568 results of *Gualandi et al.* [2014] suggesting the longer-term afterslip regions, that are also
 569 located farther away from the co-seismic ruptured zone, are characterized by a transi-
 570 tion between velocity weakening and velocity strengthening behavior. This implies that
 571 co-seismic rupture occurs and triggers early afterslip in velocity weakening regions; while

572 afterslip propagates away from the ruptured zone in fault regions that progressively be-
573 come stable with the distance to the mainshock.

574 In Figure 10, we compare the slip distributions imaged for the mainshock and 6
575 days after, with the distribution of aftershocks detected over 6 days and 9 months af-
576 ter the mainshock [Valoroso *et al.*, 2013]. As for many earthquakes, aftershocks are dis-
577 tributed mainly at the ends of the fault [Das and Henry, 2003] with few events located
578 near the co-seismic rupture. Six days after the mainshock (Figure 10a), our results show
579 no clear correlation between the location of early afterslip and aftershocks. Months af-
580 ter the mainshock, the areas with a high density of aftershocks are similar to 6 days af-
581 ter the mainshock [as suggested by Henry and Das, 2001, whereas the cumulated num-
582 ber of aftershocks is 8 times larger, see Figure S17] and the post-seismic slip has extended
583 farther away from the co-seismic rupture. This is why we can observe a spatial corre-
584 lation between some areas of long-term post-seismic slip and aftershocks [D’Agostino *et al.*,
585 2012; Cheloni *et al.*, 2014]. The spatial correlation is particularly striking for the south-
586 ern afterslip patch, for which few early aftershocks are located within the early afterslip
587 area (Figure 10a) while the aftershock cluster overlies the monthly afterslip that prop-
588 agated outward from the co-seismically ruptured zone (Figure 10b).

589 From this analysis, we can thus draw only one conclusion: there is no correlation
590 between the area of large (≥ 15 cm) early afterslip and the location of aftershocks for the
591 first few days after the mainshock. This conclusion contradicts the observations made
592 for some other earthquakes although mainly at longer time scales [e.g. Hsu *et al.*, 2006;
593 Perfettini and Avouac, 2007; Wang *et al.*, 2012; Ross *et al.*, 2017, for time periods span-
594 ning respectively 11 months, 3.5 years, 5 days and 2.5 months]. Our results could also
595 suggest that, for some parts of the fault, aftershocks nucleation precedes aseismic slip
596 which is going to occur for months after the mainshock; aftershocks could thus be partly
597 explained by stress changes due to the co-seismic rupture. But these aftershocks could
598 also be triggered by early afterslip with an amplitude so low that it is not inferred by
599 our model. The absence of clear correlation between early afterslip and aftershocks may
600 also be related to the presence of high pressure fluids in the seismogenic zone of the L’Aquila
601 event, and of Central Italy in general, with the widespread emissions of CO₂ rich fluids
602 for deep origin [Chiodini *et al.*, 2000; Frezzotti *et al.*, 2009; Chiodini *et al.*, 2011]. Already,
603 Miller *et al.* [2004] and Antonioli *et al.* [2005] proposed that the aftershocks and spatio-
604 temporal migration of the seismicity of the 1997 Umbria-Marche seismic sequence (80

605 km NE of the L'Aquila event) were driven by the co-seismically induced fluid pressure
 606 migration. Similarly, the increase in seismicity rate of the L'Aquila earthquake and the
 607 occurrence of some aftershocks may have been driven by fluid flows [Luccio *et al.*, 2010;
 608 Terakawa *et al.*, 2010; Malagnini *et al.*, 2012], as for the aftershocks migration follow-
 609 ing the 2016 Amatrice earthquake [Tung and Masterlark, 2018; Walters *et al.*, 2018]. High
 610 pressure fluids have been observed before the co-seismic rupture, and may have impacted
 611 the nucleation phase of the L'Aquila earthquake [Lucente *et al.*, 2010]. Finally, Malagnini
 612 *et al.* [2012] show that the strength of the Campotosto fault, just north of the main rup-
 613 ture (see Figure 2), has been controlled by fluid migration for at least 6 days after the
 614 mainshock, a time window corresponding to our study of early afterslip. The perturba-
 615 tions in pore fluid pressure induced by the co-seismic rupture may have triggered the first
 616 aftershocks of the L'Aquila earthquake. Fluid migration may have prevented aftershocks
 617 and early afterslip from affecting the same areas of the fault, especially if the increase
 618 in fluid pressure first produced aseismic slip, followed by triggered seismicity around the
 619 pore pressure front [Miller *et al.*, 2004]. Finally, if early aftershocks were triggered by
 620 changes in fluid pressure, it may justify the possibility that some of these early aftershocks
 621 nucleated before the occurrence of long-term afterslip in similar regions of the fault.

622 **6 Conclusion**

623 In this study, we use a simple and efficient approach to account for the differences
 624 in temporal resolution of various geodetic datasets. A redesign of the Green's Functions
 625 matrix allows us to optimize the use of the information content of datasets covering dif-
 626 ferent time periods. In particular, we propose here generic equations governing the Com-
 627 bined Time Window (CTW) approach, and detail the benefits of this approach with toy
 628 models. A comparable strategy has already been proposed by Floyd *et al.* [2016] and used
 629 in an optimization framework. With the CTW approach, we image simultaneously the
 630 strictly co-seismic slip and the early afterslip (6 days after the mainshock) of the 2009
 631 $M_w 6.3$ L'Aquila earthquake using two datasets: one covers the two slip episodes (e.g. In-
 632 SAR) while the other records the co-seismic signal only (e.g. continuous GNSS). We show
 633 that when the two phases are inverted independently, as is usually the case, the estimated
 634 slip distributions are not reliable because strictly co-seismic observations are usually of
 635 poor spatial resolution. Additionally, overlooking the early post-seismic deformation re-
 636 sults in models that overestimates the co-seismic slip, and underestimates the total post-

637 seismic slip budget. In contrast, the CTW approach allows us to accurately estimate both
638 co-seismic and early post-seismic slip models. More generally, the CTW approach will
639 also be useful to discriminate geodetic signals from earthquakes that cluster closely in
640 space and time, or from different phases of the post-seismic deformation.

641 Our results show that neglecting the contribution of the early post-seismic defor-
642 mation will likely bias estimates of the co-seismic and/or the post-seismic slip. For our
643 test case of the L'Aquila earthquake, the peak co-seismic slip is likely 30% greater when
644 early post-seismic signal is recorded as co-seismic deformation. The long-term afterslip
645 estimates are underestimated by a factor of 3 when the first 6 days of post-seismic de-
646 formation are not acknowledged. Our investigation of the L'Aquila event also stressed
647 the strong influence of uncertainties in the forward model, mainly stemming from our
648 imperfect knowledge of the fault geometry and the Earth structure, on the imaged slip
649 distributions. These uncertainties alone are sufficient to cause contradictory interpre-
650 tations on the slip history on the fault (e.g. with the existence of shallow or dip slip).

651 Our preferred slip model for the L'Aquila earthquake tends to be simpler than many
652 previous models, with one thin horizontal band of slip located around 7km depth, reach-
653 ing 150cm in amplitude near its southern end. Our model thus excludes the possibility
654 of major shallow or deep co-seismic slip patches (less than a few km or deeper than 10).
655 The early post-seismic slip (6 days after the mainshock) mostly occur in the same in-
656 termediate depth range (7 km +/- 3 km), initiating on the edges of the co-seismic slip,
657 with possibly some overlap. Some afterslip may also have occurred at greater depths.
658 A comparison with longer term afterslip models suggests that the early afterslip patches
659 might have simply expanded over time from their initial position. Aftershocks are more
660 spatially distributed (7 km +/- 5 km) but still concentrated at intermediate depth. Sev-
661 eral studies suggest that aftershocks might be driven by afterslip [e.g., *Perfettini and Avouac,*
662 *2007; Hsu et al., 2006; Sladen et al., 2010; Ross et al., 2017; Perfettini et al., 2018*] but
663 here aftershocks are only partially overlapping. This result suggests that post-seismic
664 reloading may be influenced by fluids as advocated in several previous studies [e.g., *Luc-*
665 *cio et al., 2010; Terakawa et al., 2010; Malagnini et al., 2012; Guglielmi et al., 2015; Scud-*
666 *eri and Collettini, 2016*].

667 **Acknowledgments**

668 We thank Richard Walkers for its thorough and constructive review. We thank Frederic
 669 Cappa for helpful discussions. We are extremely grateful to Federica Magnoni who shared
 670 her 3D crustal model for the L'Aquila area [*Magnoni et al.*, 2014], to Luisa Valoroso who
 671 provided the aftershock catalog for the L'Aquila earthquake [*Valoroso et al.*, 2013] and
 672 to Simone Atzori for sharing the InSAR data [*Atzori et al.*, 2009]. The Bayesian sim-
 673 ulations were performed on the HPC-Regional Center ROMEO (<https://romeo.univ-reims.fr>)
 674 of the University of Reims Champagne-Ardenne (France). The Classic Slip Inversion (CSI)
 675 Python library created by Romain Jolivet was used to build inputs for the Bayesian al-
 676 gorithm. Discussed slip models of *Gualandi et al.* [2014], *Gallovic et al.* [2015] and *Cirella*
 677 *et al.* [2012] have been retrieved from SRCMOD [<http://equake-rc.info/SRCMOD/>, *Mai*
 678 *and Thingbaijam*, 2014]. Figures were generated with the Matplotlib and Seaborn Python
 679 libraries and with the Generic Mapping Tools library. This study was partly supported
 680 by the French National Research Agency (ANR) EPOST project ANR-14-CE03-0002.
 681 Théa Ragon is supported by a fellowship from the French Ministry of Research and Higher
 682 Education.

683 **References**

- 684 Albano, M., S. Barba, M. Saroli, M. Moro, F. Malvarosa, M. Costantini, C. Big-
 685 nami, and S. Stramondo (2015), Gravity-driven postseismic deformation fol-
 686 lowing the Mw 6.3 2009 L'Aquila (Italy) earthquake, *Scientific Reports*, 5, doi:
 687 10.1038/srep16558.
- 688 Antonioli, A., D. Piccinini, L. Chiaraluce, and M. Cocco (2005), Fluid flow and seis-
 689 micity pattern: Evidence from the 1997 Umbria-Marche (central Italy) seismic
 690 sequence, *Geophysical Research Letters*, 32(10), doi:10.1029/2004GL022256.
- 691 Anzidei, M., E. Boschi, V. Cannelli, R. Devoti, A. Esposito, A. Galvani, D. Melini,
 692 G. Pietrantonio, F. Riguzzi, V. Sepe, and E. Serpelloni (2009), Coseismic deforma-
 693 tion of the destructive April 6, 2009 L'Aquila earthquake (central Italy) from GPS
 694 data, *Geophysical Research Letters*, 36(17), L17,307, doi:10.1029/2009GL039145.
- 695 Aster, R. C., B. Borchers, and C. H. Thurber (2005), *Parameter estimation and*
 696 *inverse problems*, no. 90 in International Geophysics Series, Academic Press, New
 697 York, NY.

- 698 Atzori, S., I. Hunstad, M. Chini, S. Salvi, C. Tolomei, C. Bignami, S. Stramondo,
699 E. Trasatti, A. Antonioli, and E. Boschi (2009), Finite fault inversion of DInSAR
700 coseismic displacement of the 2009 L'Aquila earthquake (central Italy), *Geophys-
701 cal Research Letters*, *36*(15), L15,305, doi:10.1029/2009GL039293.
- 702 Avallone, A., M. Marzario, A. Cirella, A. Piatanesi, A. Rovelli, C. Di Alessandro,
703 E. D'Anastasio, N. D'Agostino, R. Giuliani, and M. Mattone (2011), Very high
704 rate (10 Hz) GPS seismology for moderate-magnitude earthquakes: The case of
705 the Mw 6.3 L'Aquila (central Italy) event, *Journal of Geophysical Research: Solid
706 Earth*, *116*(B2), B02,305, doi:10.1029/2010JB007834.
- 707 Balestra, J., and B. Delouis (2015), Reassessing the Rupture Process of the 2009
708 L'Aquila Earthquake (Mw 6.3) on the Paganica Fault and Investigating the Pos-
709 sibility of Coseismic Motion on Secondary Faults, *Bulletin of the Seismological
710 Society of America*, *105*(3), 1517–1539, doi:10.1785/0120140239.
- 711 Barbot, S., and Y. Fialko (2010), A unified continuum representation of post-seismic
712 relaxation mechanisms: semi-analytic models of afterslip, poroelastic rebound
713 and viscoelastic flow, *Geophysical Journal International*, *182*(3), 1124–1140, doi:
714 10.1111/j.1365-246X.2010.04678.x.
- 715 Barnhart, W. D., C. M. J. Bregman, S. Li, and K. E. Peterson (2018), Ramp-flat
716 basement structures of the Zagros Mountains inferred from co-seismic slip and
717 afterslip of the 2017 Mw7.3 Darbandikhan, Iran/Iraq earthquake, *Earth and Plan-
718 etary Science Letters*, *496*, 96–107, doi:10.1016/j.epsl.2018.05.036.
- 719 Beresnev, I. A. (2003), Uncertainties in Finite-Fault Slip Inversions: To What Ex-
720 tent to Believe? (A Critical Review), *Bulletin of the Seismological Society of
721 America*, *93*(6), 2445–2458, doi:10.1785/0120020225.
- 722 Bletery, Q., A. Sladen, J. Jiang, and M. Simons (2016), A Bayesian source model for
723 the 2004 great Sumatra-Andaman earthquake, *Journal of Geophysical Research:
724 Solid Earth*, p. 2016JB012911, doi:10.1002/2016JB012911.
- 725 Boncio, P., G. Lavecchia, G. Milana, and B. Rozzi (2004a), Seismogenesis in Cen-
726 tral Apennines, Italy: an integrated analysis of minor earthquake sequences and
727 structural data in the Amatrice-Campotosto area, *Annals of Geophysics*, *47*(6),
728 1723–1742.
- 729 Boncio, P., G. Lavecchia, and B. Pace (2004b), Defining a model of 3d seismo-
730 genic sources for Seismic Hazard Assessment applications: The case of cen-

- 731 tral Apennines (Italy), *Journal of Seismology*, 8(3), 407–425, doi:10.1023/B:
732 JOSE.0000038449.78801.05.
- 733 Boncio, P., A. Pizzi, F. Brozzetti, G. Pomposo, G. Lavecchia, D. Di Naccio, and
734 F. Ferrarini (2010), Coseismic ground deformation of the 6 April 2009 L’Aquila
735 earthquake (central Italy, Mw6.3), *Geophysical Research Letters*, 37(6), L06,308,
736 doi:10.1029/2010GL042807.
- 737 Burgmann, R., P. Segall, M. Lisowski, and J. Svarc (1997), Postseismic strain
738 following the 1989 Loma Prieta earthquake from GPS and leveling measure-
739 ments, *Journal of Geophysical Research: Solid Earth*, 102(B3), 4933–4955, doi:
740 10.1029/96JB03171.
- 741 Causse, M., F. Cotton, and P. M. Mai (2010), Constraining the roughness degree
742 of slip heterogeneity, *Journal of Geophysical Research: Solid Earth*, 115(B5),
743 doi:10.1029/2009JB006747.
- 744 Chan, C.-H., and R. S. Stein (2009), Stress evolution following the 1999 Chi-Chi,
745 Taiwan, earthquake: Consequences for afterslip, relaxation, aftershocks and de-
746 partures from Omori decay, *Geophysical Journal International*, 177(1), 179–192,
747 doi:10.1111/j.1365-246X.2008.04069.x.
- 748 Cheloni, D., N. D’Agostino, E. D’Anastasio, A. Avallone, S. Mantenuto, R. Giu-
749 liani, M. Mattone, S. Calcaterra, P. Gambino, D. Dominici, F. Radicioni, and
750 G. Fastellini (2010), Coseismic and initial post-seismic slip of the 2009 Mw 6.3
751 L’Aquila earthquake, Italy, from GPS measurements, *Geophysical Journal Inter-
752 national*, 181(3), 1539–1546, doi:10.1111/j.1365-246X.2010.04584.x.
- 753 Cheloni, D., R. Giuliani, E. D’Anastasio, S. Atzori, R. J. Walters, L. Bonci,
754 N. D’Agostino, M. Mattone, S. Calcaterra, P. Gambino, F. Deninno, R. Maseroli,
755 and G. Stefanelli (2014), Coseismic and post-seismic slip of the 2009 L’Aquila
756 (central Italy) MW 6.3 earthquake and implications for seismic potential along the
757 Campotosto fault from joint inversion of high-precision levelling, InSAR and GPS
758 data, *Tectonophysics*, 622, 168–185, doi:10.1016/j.tecto.2014.03.009.
- 759 Chiarabba, C., A. Amato, M. Anselmi, P. Baccheschi, I. Bianchi, M. Cattaneo,
760 G. Cecere, L. Chiaraluce, M. G. Ciaccio, P. De Gori, G. De Luca, M. Di Bona,
761 R. Di Stefano, L. Faenza, A. Govoni, L. Improta, F. P. Lucente, A. Marchetti,
762 L. Margheriti, F. Mele, A. Michelini, G. Monachesi, M. Moretti, M. Pastori, N. Pi-
763 ana Agostinetti, D. Piccinini, P. Roselli, D. Seccia, and L. Valoroso (2009), The

- 764 2009 L'Aquila (central Italy) MW6.3 earthquake: Main shock and aftershocks,
765 *Geophysical Research Letters*, *36*(18), L18,308, doi:10.1029/2009GL039627.
- 766 Chiaraluce, L. (2012), Unravelling the complexity of Apenninic extensional fault
767 systems: A review of the 2009 L'Aquila earthquake (Central Apennines, Italy),
768 *Journal of Structural Geology*, *42*, 2–18, doi:10.1016/j.jsg.2012.06.007.
- 769 Chiaraluce, L., L. Valoroso, D. Piccinini, R. Di Stefano, and P. De Gori (2011), The
770 anatomy of the 2009 L'Aquila normal fault system (central Italy) imaged by high
771 resolution foreshock and aftershock locations, *Journal of Geophysical Research:*
772 *Solid Earth*, *116*(B12), B12,311, doi:10.1029/2011JB008352.
- 773 Chiodini, G., F. Frondini, C. Cardellini, F. Parello, and L. Peruzzi (2000), Rate of
774 diffuse carbon dioxide Earth degassing estimated from carbon balance of regional
775 aquifers: The case of central Apennine, Italy, *Journal of Geophysical Research:*
776 *Solid Earth*, *105*(B4), 8423–8434, doi:10.1029/1999JB900355.
- 777 Chiodini, G., S. Caliro, C. Cardellini, F. Frondini, S. Inguaggiato, and F. Matteucci
778 (2011), Geochemical evidence for and characterization of CO₂ rich gas sources in
779 the epicentral area of the Abruzzo 2009 earthquakes, *Earth and Planetary Science*
780 *Letters*, *304*(3), 389–398, doi:10.1016/j.epsl.2011.02.016.
- 781 Chlieh, M., J.-P. Avouac, V. Hjorleifsdottir, T.-R. A. Song, C. Ji, K. Sieh,
782 A. Sladen, H. Hebert, L. Prawirodirdjo, Y. Bock, and J. Galetzka (2007), Co-
783 seismic Slip and Afterslip of the Great Mw 9.15 SumatraAndaman Earthquake
784 of 2004, *Bulletin of the Seismological Society of America*, *97*(1A), S152–S173,
785 doi:10.1785/0120050631.
- 786 Cirella, A., A. Piatanesi, E. Tinti, M. Chini, and M. Cocco (2012), Complexity of
787 the rupture process during the 2009 L'Aquila, Italy, earthquake, *Geophysical*
788 *Journal International*, *190*(1), 607–621, doi:10.1111/j.1365-246X.2012.05505.x.
- 789 Cubas, N., N. Lapusta, J.-P. Avouac, and H. Perfettini (2015), Numerical modeling
790 of long-term earthquake sequences on the NE Japan megathrust: Comparison
791 with observations and implications for fault friction, *Earth and Planetary Science*
792 *Letters*, *419*(Supplement C), 187–198, doi:10.1016/j.epsl.2015.03.002.
- 793 D'Agostino, N., D. Cheloni, G. Fornaro, R. Giuliani, and D. Reale (2012), Space-
794 time distribution of afterslip following the 2009 L'Aquila earthquake, *Journal of*
795 *Geophysical Research: Solid Earth*, *117*(B2), B02,402, doi:10.1029/2011JB008523.

- 796 Das, S., and C. Henry (2003), Spatial relation between main earthquake slip and its
797 aftershock distribution, *Reviews of Geophysics*, *41*(3), doi:10.1029/2002RG000119.
- 798 Delouis, B., D. Giardini, P. Lundgren, and J. Salichon (2002), Joint Inversion of
799 InSAR, GPS, Telesismic, and Strong-Motion Data for the Spatial and Tem-
800 poral Distribution of Earthquake Slip: Application to the 1999 izmit Main-
801 shock, *Bulletin of the Seismological Society of America*, *92*(1), 278–299, doi:
802 10.1785/0120000806.
- 803 Dieterich, J. (1994), A constitutive law for rate of earthquake production and its ap-
804 plication to earthquake clustering, *Journal of Geophysical Research: Solid Earth*,
805 *99*(B2), 2601–2618, doi:10.1029/93JB02581.
- 806 Du, Y., A. Aydin, and P. Segall (1992), Comparison of various inversion techniques
807 as applied to the determination of a geophysical deformation model for the 1983
808 Borah Peak earthquake, *Bulletin of the Seismological Society of America*, *82*(4),
809 1840–1866.
- 810 Duputel, Z., P. S. Agram, M. Simons, S. E. Minson, and J. L. Beck (2014), Account-
811 ing for prediction uncertainty when inferring subsurface fault slip, *Geophysical*
812 *journal international*, *197*(1), 464–482.
- 813 Elliott, J. R., A. C. Copley, R. Holley, K. Scharer, and B. Parsons (2013), The 2011
814 Mw 7.1 Van (Eastern Turkey) earthquake, *Journal of Geophysical Research: Solid*
815 *Earth*, *118*(4), 1619–1637, doi:10.1002/jgrb.50117.
- 816 EMERGEO Working Group (2010), Evidence for surface rupture associated with the
817 Mw 6.3 L’Aquila earthquake sequence of April 2009 (central Italy), *Terra Nova*,
818 *22*(1), 43–51, doi:10.1111/j.1365-3121.2009.00915.x.
- 819 Falcucci, E., S. Gori, E. Peronace, G. Fubelli, M. Moro, M. Saroli, B. Giaccio,
820 P. Messina, G. Naso, G. Scardia, A. Sposato, M. Voltaggio, P. Galli, and F. Gal-
821 adini (2009), The Paganica Fault and Surface Coseismic Ruptures Caused by the
822 6 April 2009 Earthquake (L’Aquila, Central Italy), *Seismological Research Letters*,
823 *80*(6), 940–950, doi:10.1785/gssrl.80.6.940.
- 824 Floyd, M. A., R. J. Walters, J. R. Elliott, G. J. Funning, J. L. Svarc, J. R. Murray,
825 A. J. Hooper, Y. Larsen, P. Marinkovic, R. Brgmann, I. A. Johanson, and T. J.
826 Wright (2016), Spatial variations in fault friction related to lithology from rup-
827 ture and afterslip of the 2014 South Napa, California, earthquake, *Geophysical*
828 *Research Letters*, *43*(13), 6808–6816, doi:10.1002/2016GL069428.

- 829 Freed, A. M. (2007), Afterslip (and only afterslip) following the 2004 Parkfield,
830 California, earthquake, *Geophysical Research Letters*, *34*(6), L06,312, doi:
831 10.1029/2006GL029155.
- 832 Freed, A. M., and R. Burgmann (2004), Evidence of power-law flow in the Mojave
833 desert mantle, *Nature*, *430*(6999), 548–51.
- 834 Frezzotti, M. L., A. Peccerillo, and G. Panza (2009), Carbonate metasomatism and
835 CO₂ lithosphereasthenosphere degassing beneath the Western Mediterranean:
836 An integrated model arising from petrological and geophysical data, *Chemical*
837 *Geology*, *262*(1), 108–120, doi:10.1016/j.chemgeo.2009.02.015.
- 838 Gallovic, F., W. Imperatori, and P. M. Mai (2015), Effects of three-dimensional
839 crustal structure and smoothing constraint on earthquake slip inversions: Case
840 study of the Mw6.3 2009 L’Aquila earthquake, *Journal of Geophysical Research:*
841 *Solid Earth*, *120*(1), 2014JB011,650, doi:10.1002/2014JB011650.
- 842 Gombert, B., Z. Duputel, R. Jolivet, C. Doubre, L. Rivera, and M. Simons (2017),
843 Revisiting the 1992 Landers earthquake: a Bayesian exploration of co-seismic slip
844 and off-fault damage, *Geophysical Journal International*, doi:10.1093/gji/ggx455.
- 845 Gualandi, A., E. Serpelloni, and M. E. Belardinelli (2014), Space-time evolution
846 of crustal deformation related to the Mw 6.3, 2009 L’Aquila earthquake (central
847 Italy) from principal component analysis inversion of GPS position time-series,
848 *Geophysical Journal International*, p. ggt522, doi:10.1093/gji/ggt522.
- 849 Gualandi, A., J.-P. Avouac, J. Galetzka, J. F. Genrich, G. Blewitt, L. B. Ad-
850 hikari, B. P. Koirala, R. Gupta, B. N. Upreti, B. Pratt-Sitaula, and J. Liu-
851 Zeng (2017), Pre- and post-seismic deformation related to the 2015, Mw7.8
852 Gorkha earthquake, Nepal, *Tectonophysics*, *714*(Supplement C), 90–106, doi:
853 10.1016/j.tecto.2016.06.014.
- 854 Guglielmi, Y., F. Cappa, J.-P. Avouac, P. Henry, and D. Elsworth (2015), Seismicity
855 triggered by fluid injectioninduced aseismic slip, *Science*, *348*(6240), 1224–1226,
856 doi:10.1126/science.aab0476.
- 857 He, P., E. A. Hetland, Q. Wang, K. Ding, Y. Wen, and R. Zou (2017), Coseis-
858 mic Slip in the 2016 Mw 7.8 Ecuador Earthquake Imaged from Sentinel-1a
859 Radar Interferometry, *Seismological Research Letters*, *88*(2A), 277–286, doi:
860 10.1785/0220160151.

- 861 Helmstetter, A., and B. E. Shaw (2009), Afterslip and aftershocks in the rate-and-
862 state friction law, *Journal of Geophysical Research: Solid Earth*, *114*(B1), doi:
863 10.1029/2007JB005077.
- 864 Henry, C., and S. Das (2001), Aftershock zones of large shallow earthquakes: fault
865 dimensions, aftershock area expansion and scaling relations, *Geophysical Journal*
866 *International*, *147*(2), 272–293, doi:10.1046/j.1365-246X.2001.00522.x.
- 867 Herrmann, R. B., L. Malagnini, and I. Munafo (2011), Regional Moment Tensors of
868 the 2009 L’Aquila Earthquake Sequence, *Bulletin of the Seismological Society of*
869 *America*, *101*(3), 975–993, doi:10.1785/0120100184.
- 870 Hsu, Y.-J., M. Simons, J.-P. Avouac, J. Galetzka, K. Sieh, M. Chlieh, D. Nataw-
871 idjaja, L. Prawirodirdjo, and Y. Bock (2006), Frictional Afterslip Following the
872 2005 Nias-Simeulue Earthquake, Sumatra, *Science*, *312*(5782), 1921–1926, doi:
873 10.1126/science.1126960.
- 874 Johnson, K. M., J. Fukuda, and P. Segall (2012), Challenging the rate-state asperity
875 model: Afterslip following the 2011 M9 Tohoku-oki, Japan, earthquake, *Geophysi-*
876 *cal Research Letters*, *39*(20), L20,302, doi:10.1029/2012GL052901.
- 877 Jolivet, R., C. Lasserre, M.-P. Doin, S. Guillaso, G. Peltzer, R. Dailu, J. Sun, Z.-
878 K. Shen, and X. Xu (2012), Shallow creep on the Haiyuan Fault (Gansu, China)
879 revealed by SAR Interferometry, *Journal of Geophysical Research: Solid Earth*,
880 *117*(B6), B06,401, doi:10.1029/2011JB008732.
- 881 Jonsson, S., P. Segall, R. Pedersen, and G. Bjornsson (2003), Post-earthquake
882 ground movements correlated to pore-pressure transients, *Nature*, *424*(6945),
883 179–83.
- 884 Kato, A., K. Obara, T. Igarashi, H. Tsuruoka, S. Nakagawa, and N. Hirata (2012),
885 Propagation of Slow Slip Leading Up to the 2011 Mw 9.0 Tohoku-Oki Earthquake,
886 *Science*, *335*(6069), 705–708, doi:10.1126/science.1215141.
- 887 Lavecchia, G., F. Ferrarini, F. Brozzetti, R. D. Nardis, P. Boncio, and L. Chiaraluce
888 (2012), From surface geology to aftershock analysis: Constraints on the geometry
889 of the L’Aquila 2009 seismogenic fault system, *Italian Journal of Geosciences*,
890 *131*(3), 330–347, doi:10.3301/IJG.2012.24.
- 891 Lin, Y.-n. N., A. Sladen, F. Ortega-Culaciati, M. Simons, J.-P. Avouac, E. J. Field-
892 ing, B. A. Brooks, M. Bevis, J. Genrich, A. Rietbrock, C. Vigny, R. Smalley, and
893 A. Socquet (2013), Coseismic and postseismic slip associated with the 2010 Maule

- 894 Earthquake, Chile: Characterizing the Arauco Peninsula barrier effect, *Journal of*
895 *Geophysical Research: Solid Earth*, *118*(6), 3142–3159, doi:10.1002/jgrb.50207.
- 896 Lohman, R. B., and M. Simons (2005), Some thoughts on the use of InSAR
897 data to constrain models of surface deformation: Noise structure and data
898 downsampling, *Geochemistry, Geophysics, Geosystems*, *6*(1), Q01,007, doi:
899 10.1029/2004GC000841.
- 900 Luccio, F. D., G. Ventura, R. D. Giovambattista, A. Piscini, and F. R. Cinti (2010),
901 Normal faults and thrusts reactivated by deep fluids: The 6 April 2009 Mw 6.3
902 L’Aquila earthquake, central Italy, *Journal of Geophysical Research: Solid Earth*,
903 *115*(B6), doi:10.1029/2009JB007190.
- 904 Lucente, F. P., P. D. Gori, L. Margheriti, D. Piccinini, M. D. Bona, C. Chiarabba,
905 and N. P. Agostinetti (2010), Temporal variation of seismic velocity and
906 anisotropy before the 2009 MW 6.3 L’Aquila earthquake, Italy, *Geology*, *38*(11),
907 1015–1018, doi:10.1130/G31463.1.
- 908 Magnoni, F., E. Casarotti, A. Michelini, A. Piersanti, D. Komatitsch, D. Peter, and
909 J. Tromp (2014), Spectral Element Simulations of Seismic Waves Generated by
910 the 2009 L’Aquila Earthquake, *Bulletin of the Seismological Society of America*,
911 *104*(1), 73–94, doi:10.1785/0120130106.
- 912 Mai, P. M., and K. K. S. Thingbaijam (2014), SRCMOD: An Online Database of
913 Finite-Fault Rupture Models, *Seismological Research Letters*, *85*(6), 1348–1357,
914 doi:10.1785/0220140077.
- 915 Malagnini, L., F. P. Lucente, P. D. Gori, A. Akinci, and I. Munafo’ (2012), Con-
916 trol of pore fluid pressure diffusion on fault failure mode: Insights from the 2009
917 L’Aquila seismic sequence, *Journal of Geophysical Research: Solid Earth*, *117*(B5),
918 doi:10.1029/2011JB008911.
- 919 Malservisi, R., S. Y. Schwartz, N. Voss, M. Protti, V. Gonzalez, T. H. Dixon,
920 Y. Jiang, A. V. Newman, J. Richardson, J. I. Walter, and D. Vayenko (2015),
921 Multiscale postseismic behavior on a megathrust: The 2012 Nicoya earthquake,
922 Costa Rica, *Geochemistry, Geophysics, Geosystems*, *16*(6), 1848–1864, doi:
923 10.1002/2015GC005794.
- 924 Marone, C. J., C. H. Scholtz, and R. Bilham (1991), On the mechanics of earth-
925 quake afterslip, *Journal of Geophysical Research: Solid Earth*, *96*(B5), 8441–8452,
926 doi:10.1029/91JB00275.

- 927 Miller, S. A., C. Collettini, L. Chiaraluce, M. Cocco, M. Barchi, and B. J. P. Kaus
928 (2004), Aftershocks driven by a high-pressure CO₂ source at depth, *Nature*,
929 *427*(6976), 724–727, doi:10.1038/nature02251.
- 930 Minson, S. E., M. Simons, and J. L. Beck (2013), Bayesian inversion for finite fault
931 earthquake source models I: theory and algorithm, *Geophysical Journal Interna-*
932 *tional*, *194*(3), 1701–1726, doi:10.1093/gji/ggt180.
- 933 Miyazaki, S., P. Segall, J. Fukuda, and T. Kato (2004), Space time distribution of
934 afterslip following the 2003 Tokachi-oki earthquake: Implications for variations
935 in fault zone frictional properties, *Geophysical Research Letters*, *31*(6), L06,623,
936 doi:10.1029/2003GL019410.
- 937 Munekane, H. (2012), Coseismic and early postseismic slips associated with
938 the 2011 off the Pacific coast of Tohoku Earthquake sequence: EOF analy-
939 sis of GPS kinematic time series, *Earth, Planets and Space*, *64*(12), 3, doi:
940 10.5047/eps.2012.07.009.
- 941 Nur, A., and G. Mavko (1974), Postseismic Viscoelastic Rebound, *Science*,
942 *183*(4121), 204–206, doi:10.1126/science.183.4121.204.
- 943 Parzen, E. (1962), On Estimation of a Probability Density Function and Mode, *The*
944 *Annals of Mathematical Statistics*, *33*(3), 1065–1076.
- 945 Peltzer, G., P. Rosen, F. Rogez, and K. Hudnut (1998), Poroelastic rebound along
946 the Landers 1992 earthquake surface rupture, *Journal of Geophysical Research:*
947 *Solid Earth*, *103*(B12), 30,131–30,145, doi:10.1029/98JB02302.
- 948 Peng, Z., and P. Zhao (2009), Migration of early aftershocks following the 2004
949 Parkfield earthquake, *Nature Geoscience*, *2*, 877–881, doi:10.1038/ngeo697.
- 950 Perfettini, H., and J.-P. Avouac (2004), Postseismic relaxation driven by brittle
951 creep: A possible mechanism to reconcile geodetic measurements and the decay
952 rate of aftershocks, application to the Chi-Chi earthquake, Taiwan, *Journal of*
953 *Geophysical Research: Solid Earth*, *109*(B2), B02,304, doi:10.1029/2003JB002488.
- 954 Perfettini, H., and J.-P. Avouac (2007), Modeling afterslip and aftershocks follow-
955 ing the 1992 Landers earthquake, *Journal of Geophysical Research: Solid Earth*,
956 *112*(B7), B07,409, doi:10.1029/2006JB004399.
- 957 Perfettini, H., and J. P. Avouac (2014), The seismic cycle in the area of the 2011
958 Mw9.0 Tohoku-Oki earthquake, *Journal of Geophysical Research: Solid Earth*,
959 *119*(5), 4469–4515, doi:10.1002/2013JB010697.

- 960 Perfettini, H., W. B. Frank, D. Marsan, and M. Bouchon (2018), A Model of Af-
961 tershock Migration Driven by Afterslip, *Geophysical Research Letters*, *45*(5),
962 2283–2293, doi:10.1002/2017GL076287.
- 963 Pollitz, F. F., R. Burgmann, and P. Segall (1998), Joint estimation of afterslip
964 rate and postseismic relaxation following the 1989 Loma Prieta earthquake,
965 *Journal of Geophysical Research: Solid Earth*, *103*(B11), 26,975–26,992, doi:
966 10.1029/98JB01554.
- 967 Pondrelli, S., S. Salimbeni, A. Morelli, G. Ekstrom, M. Olivieri, and E. Boschi
968 (2010), Seismic moment tensors of the April 2009, L’Aquila (Central Italy),
969 earthquake sequence, *Geophysical Journal International*, *180*(1), 238–242, doi:
970 10.1111/j.1365-246X.2009.04418.x.
- 971 Ragon, T., A. Sladen, and M. Simons (2018), Accounting for uncertain fault ge-
972 ometry in earthquake source inversions - I: theory and simplified application,
973 *Geophysical Journal International*, *214*(2), 1174–1190, doi:10.1093/gji/ggy187.
- 974 Ragon, T., A. Sladen, and M. Simons (2019), Accounting for uncertain
975 fault geometry in earthquake source inversions II: application to the
976 $\{\mathrm{M}_w\}$ 6.2 Amatrice earthquake, Central Italy, *Geo-*
977 *physical Journal International*, doi:10.1093/gji/ggz180.
- 978 Rice, J., and A. L. Ruina (1983), *Stability of Steady Frictional Slipping*, vol. 50,
979 doi:10.1115/1.3167042.
- 980 Rosen, P. A., S. Henley, G. Peltzer, and M. Simons (2004), Update Repeat
981 Orbit Interferometry Package Released, *EOS Transactions*, *85*, 47–47, doi:
982 10.1029/2004EO050004.
- 983 Ross, Z. E., C. Rollins, E. S. Cochran, E. Hauksson, J.-P. Avouac, and Y. Ben-Zion
984 (2017), Aftershocks driven by afterslip and fluid pressure sweeping through a
985 fault-fracture mesh, *Geophysical Research Letters*, *44*(16), 2017GL074634, doi:
986 10.1002/2017GL074634.
- 987 Ruiz, S., M. Metois, A. Fuenzalida, J. Ruiz, F. Leyton, R. Grandin, C. Vigny,
988 R. Madariaga, and J. Campos (2014), Intense foreshocks and a slow slip event
989 preceded the 2014 Iquique Mw 8.1 earthquake, *Science*, *345*(6201), 1165–1169,
990 doi:10.1126/science.1256074.
- 991 Salman, R., E. M. Hill, L. Feng, E. O. Lindsey, D. Mele Veedu, S. Barbot, P. Baner-
992 jee, I. Hermawan, and D. H. Natawidjaja (2017), Piecemeal Rupture of the

- 993 Mentawai Patch, Sumatra: The 2008 Mw 7.2 North Pagai Earthquake Se-
 994 quence, *Journal of Geophysical Research: Solid Earth*, 122(11), 9404–9419, doi:
 995 10.1002/2017JB014341.
- 996 Scognamiglio, L., E. Tinti, and A. Michelini (2009), Real-Time Determination of
 997 Seismic Moment Tensor for the Italian Region, *Bulletin of the Seismological Soci-
 998 ety of America*, 99(4), 2223–2242, doi:10.1785/0120080104.
- 999 Scuderi, M. M., and C. Collettini (2016), The role of fluid pressure in induced vs.
 1000 triggered seismicity: insights from rock deformation experiments on carbonates,
 1001 *Scientific Reports*, 6, 24,852, doi:10.1038/srep24852.
- 1002 Segall, P. (2010), *Earthquake and Volcano Deformation*, Princeton University Press,
 1003 google-Books-ID: x6Fp4hMBTpYC.
- 1004 Serpelloni, E., L. Anderlini, and M. E. Belardinelli (2012), Fault geometry,
 1005 coseismic-slip distribution and Coulomb stress change associated with the 2009
 1006 April 6, Mw 6.3, L’Aquila earthquake from inversion of GPS displacements, *Geo-
 1007 physical Journal International*, 188(2), 473–489, doi:10.1111/j.1365-246X.2011.
 1008 05279.x.
- 1009 Sladen, A., H. Tavera, M. Simons, J. P. Avouac, A. O. Konca, H. Perfettini, L. Au-
 1010 din, E. J. Fielding, F. Ortega, and R. Cavagnoud (2010), Source model of the
 1011 2007 Mw 8.0 Pisco, Peru earthquake: Implications for seismogenic behavior of
 1012 subduction megathrusts, *Journal of Geophysical Research: Solid Earth*, 115(B2),
 1013 B02,405, doi:10.1029/2009JB006429.
- 1014 Smith, B., and D. Sandwell (2004), A three-dimensional semianalytic viscoelastic
 1015 model for time-dependent analyses of the earthquake cycle, *Journal of Geophysical
 1016 Research: Solid Earth*, 109(B12), B12,401, doi:10.1029/2004JB003185.
- 1017 Terakawa, T., A. Zoporowski, B. Galvan, and S. A. Miller (2010), High-pressure
 1018 fluid at hypocentral depths in the L’Aquila region inferred from earthquake focal
 1019 mechanisms, *Geology*, 38(11), 995–998, doi:10.1130/G31457.1.
- 1020 Trasatti, E., C. Kyriakopoulos, and M. Chini (2011), Finite element inversion of
 1021 DInSAR data from the Mw 6.3 L’Aquila earthquake, 2009 (Italy), *Geophysical
 1022 Research Letters*, 38(8), L08,306, doi:10.1029/2011GL046714.
- 1023 Tung, S., and T. Masterlark (2018), Resolving Source Geometry of the 24 August
 1024 2016 Amatrice, Central Italy, Earthquake from InSAR Data and 3d FiniteEle-
 1025 ment Modeling, *Bulletin of the Seismological Society of America*, 108(2), 553–572,

- 1026 doi:10.1785/0120170139.
- 1027 Twardzik, C., M. Vergnolle, A. Sladen, and A. Avallone (2019), Unravelling the con-
1028 tribution of early postseismic deformation using sub-daily GNSS positioning —,
1029 *Scientific Reports*, *9*(1), 1775, doi:10.1038/s41598-019-39038-z.
- 1030 Valoroso, L., L. Chiaraluce, D. Piccinini, R. Di Stefano, D. Schaff, and F. Wald-
1031 hauser (2013), Radiography of a normal fault system by 64,000 high-precision
1032 earthquake locations: The 2009 L'Aquila (central Italy) case study, *Journal of*
1033 *Geophysical Research: Solid Earth*, *118*(3), 1156–1176, doi:10.1002/jgrb.50130.
- 1034 Vittori, E., P. D. Manna, A. M. Blumetti, V. Comerci, L. Guerrieri, E. Esposito,
1035 A. M. Michetti, S. Porfido, L. Piccardi, G. P. Roberts, A. Berlusconi, F. Livio,
1036 G. Sileo, M. Wilkinson, K. J. W. McCaffrey, R. J. Phillips, and P. A. Cowie
1037 (2011), Surface Faulting of the 6 April 2009 Mw 6.3 L'Aquila Earthquake in
1038 Central Italy, *Bulletin of the Seismological Society of America*, *101*(4), 1507–1530,
1039 doi:10.1785/0120100140.
- 1040 Volpe, M., A. Piersanti, and D. Melini (2012), Complex 3-D Finite Element mod-
1041 elling of the 2009 April 6 L'Aquila earthquake by inverse analysis of static
1042 deformation, *Geophysical Journal International*, *188*(3), 1339–1358, doi:
1043 10.1111/j.1365-246X.2011.05330.x.
- 1044 Volpe, M., S. Atzori, A. Piersanti, and D. Melini (2015), The 2009 L'Aquila earth-
1045 quake coseismic rupture: open issues and new insights from 3d finite element
1046 inversion of GPS, InSAR and strong motion data, *Annals of Geophysics*, *58*(2),
1047 S0221, doi:10.4401/ag-6711.
- 1048 Walters, R. J., L. C. Gregory, L. N. J. Wedmore, T. J. Craig, K. McCaffrey,
1049 M. Wilkinson, J. Chen, Z. Li, J. R. Elliott, H. Goodall, F. Iezzi, F. Livio, A. M.
1050 Michetti, G. Roberts, and E. Vittori (2018), Dual control of fault intersections on
1051 stop-start rupture in the 2016 Central Italy seismic sequence, *Earth and Planetary*
1052 *Science Letters*, *500*, 1–14, doi:10.1016/j.epsl.2018.07.043.
- 1053 Wang, L., S. Hainzl, G. Zoller, and M. Holschneider (2012), Stress- and aftershock-
1054 constrained joint inversions for coseismic and postseismic slip applied to the
1055 2004 M6.0 Parkfield earthquake, *Journal of Geophysical Research: Solid Earth*,
1056 *117*(B7), B07,406, doi:10.1029/2011JB009017.
- 1057 Yano, T. E., G. Shao, Q. Liu, C. Ji, and R. J. Archuleta (2014), Coseismic and po-
1058 tential early afterslip distribution of the 2009 Mw 6.3 L'Aquila, Italy earthquake,

1059 *Geophysical Journal International*, 199(1), 23–40, doi:10.1093/gji/ggu241.
 1060 Zhu, L., and L. A. Rivera (2002), A note on the dynamic and static displacements
 1061 from a point source in multilayered media, *Geophysical Journal International*,
 1062 148(3), 619–627, doi:10.1046/j.1365-246X.2002.01610.x.

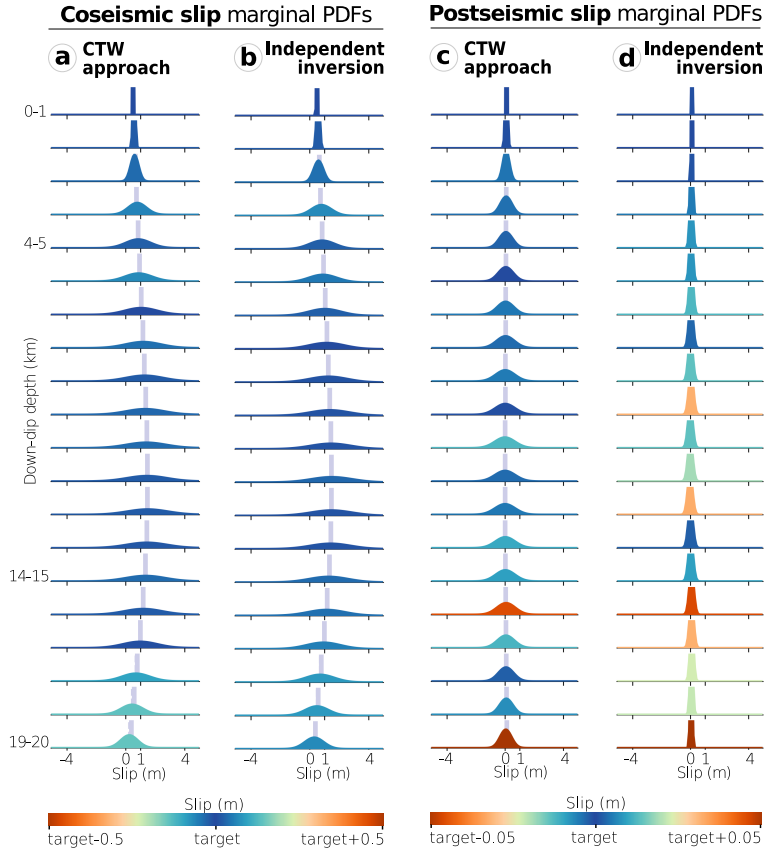


Figure 1. Co-seismic and post-seismic slip inferred for the simplified case of a fault that extends infinitely along strike. The co- and post-seismic slip models inferred from the CTW approach are shown in (a) and (c), and can be compared to the slip inferred from the inversion of co-seismic data only (b) and the post-seismic slip distribution (d) resulting from the difference between slip inferred from the inversion of co+post data and slip of (b). The fault is discretized along dip in 20 subfaults, and the input slip (i.e. the target) for each subfault is represented as a gray vertical line. For each subfault, the posterior PDFs of co-seismic (a and b) and post-seismic (c and d) slip is colored according to the offset between the target parameter and the posterior mean, with a colorscale saturated at 50 cm for the co-seismic slip and at 5 cm for the post-seismic slip. The target slip is well inferred if the PDF of a particular parameter is colored in dark blue, while it is not if the PDF is colored in red.

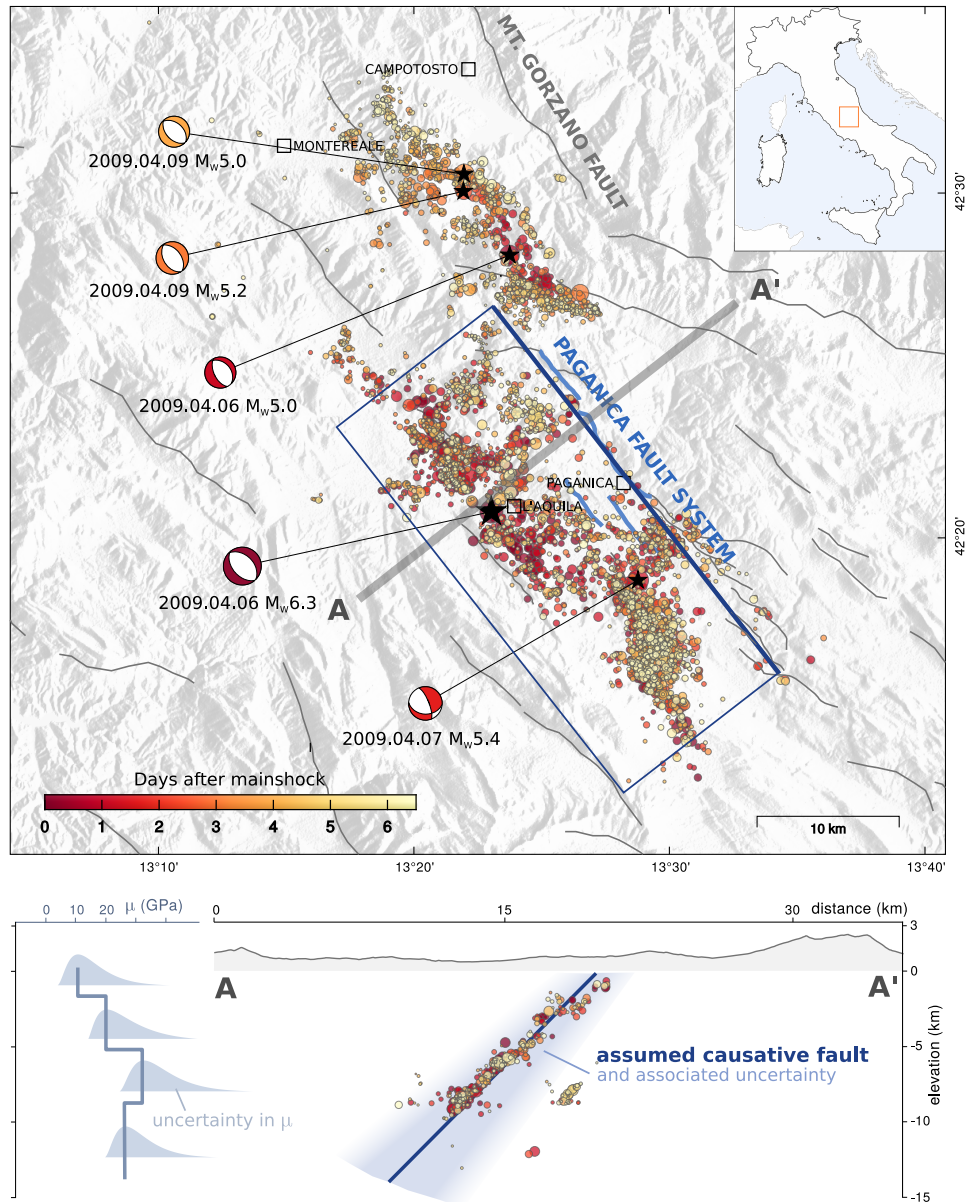


Figure 2. Seismotectonic framework of the area involved in the 2009 seismic sequence (top) and assumed forward model and associated uncertainties (bottom). In the map, coloured circles are the aftershocks from 2009 April 6 at 01:32 UTC to 2009 April 12, from the catalog of *Valoroso et al.* [2013]. The aftershocks are coloured from their occurrence time after the mainshock. Beach balls are the focal mechanisms of the mainshock and four main aftershocks, with their respective epicenters located by black stars. Solid gray lines are the major seismogenic faults of the area [Boncio *et al.*, 2004a; Lavecchia *et al.*, 2012]. The observed co-seismic surface rupture is indicated with continuous blue lines [Boncio *et al.*, 2010]. Our assumed fault geometry is shown with a dark blue rectangle. In the elevation profile (bottom), uncertainty in the fault geometry is illustrated in blue. The assumed elastic modulus μ and associated uncertainties are also illustrated for the 12 first kilometers below the Earth surface.

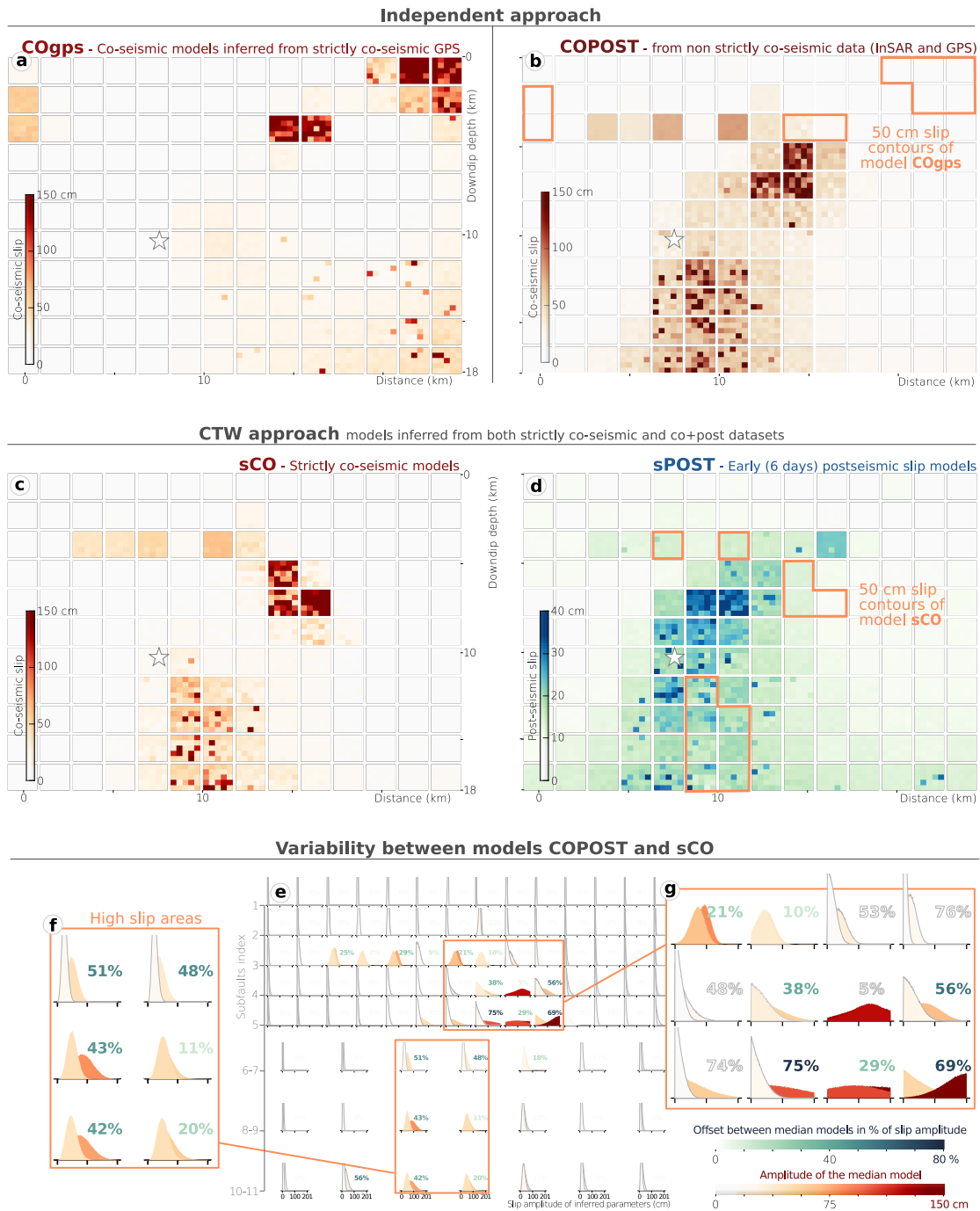


Figure 3. Comparison between finite-fault models inferred with the independent or the CTW approach. (a) Strictly co-seismic (30 s after the mainshock) slip model, named COgps, inferred from the strictly co-seismic dataset (GPS only). (b) Non-strictly co-seismic model COPOST inferred from the co-seismic dataset contaminated with some post-seismic deformation. (c) and (d) Strictly co-seismic sCO and early postseismic sPOST (6 days after the mainshock) slip models inferred jointly with the CTW approach. (a) to (d) illustrate the slip amplitude of the median models (sum of strike- and dip-slip component) of 25 families of inferred models (more information in the text and Figure S3). Each subfault (large square) is divided into 25 pixels colored from the slip amplitude of the corresponding median model. (e) Comparison between the posterior Probability Density Functions of the dip-slip parameters of models COPOST (b) and sCO (c), colored from the amplitude of their median model. In the last four rows, the PDFs have been merged, covering 2 subfaults along strike and 2 subfaults along dip (i.e. patches two times bigger

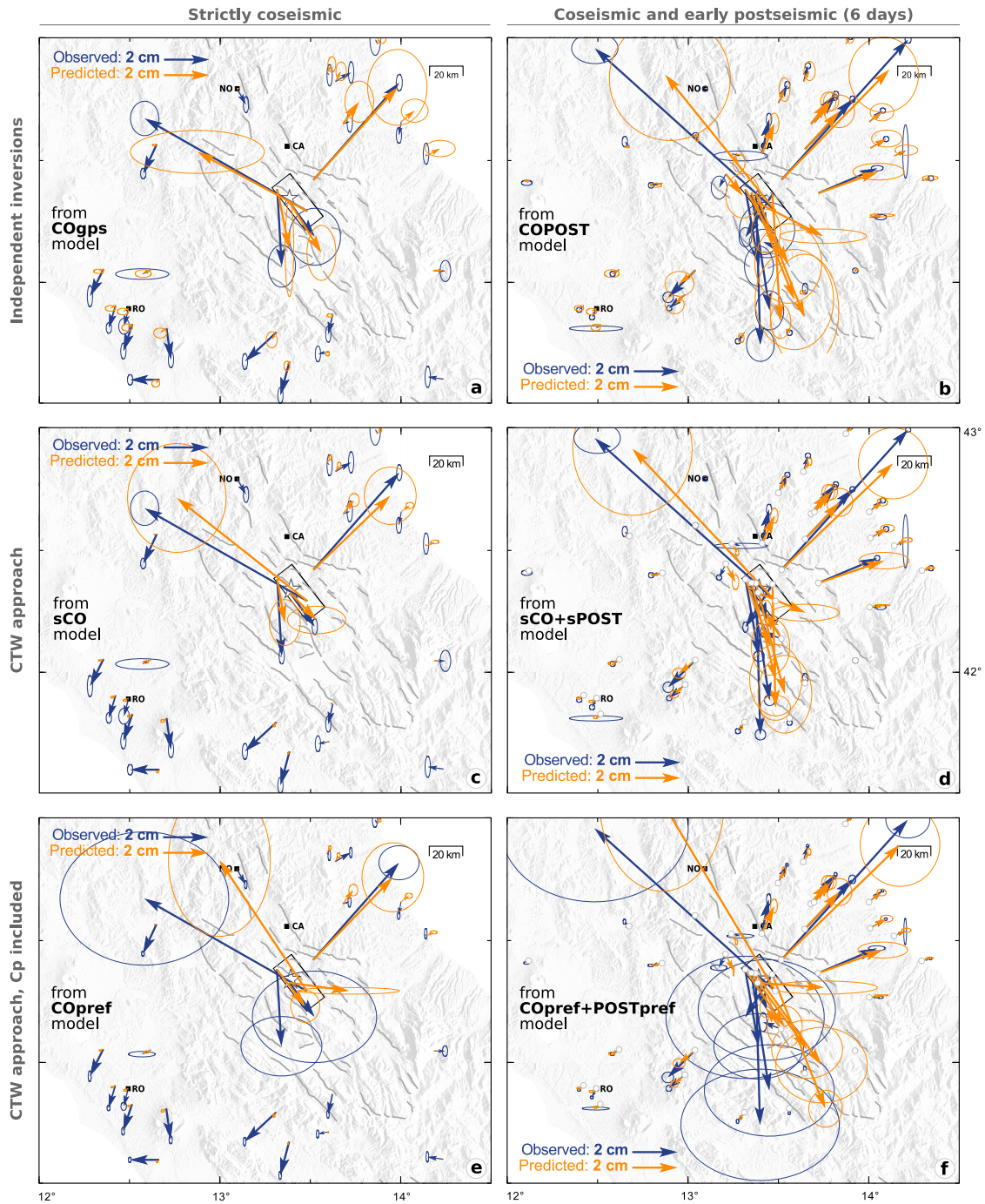


Figure 4. Comparison of horizontal surface displacement at GPS stations. Strictly co-seismic displacement is shown on the left while "co+post" displacement is shown on the right. Observed surface displacement is in blue with 95% confidence ellipses. Predictions are in orange with 95% confidence ellipses. In the top and middle rows, observational confidence ellipses (in blue) include only data errors. (a) and (b) The predictions have been calculated independently: using "co" data (a) and the "co+post" dataset (b). In (c) and (d), predictions are derived from the CTW approach. (e) and (f) show the predictions for a similar inversion setup, except epistemic uncertainties have been added to the data errors, enlarging the confidence ellipses. Our fault geometry is shown with a black rectangular box. The cities of Norcia (NO), Campotosto (CA) and Roma (RO) are indicated with black squares. Major seismogenic faults are shown in gray solid lines and the epicenter is the white star.

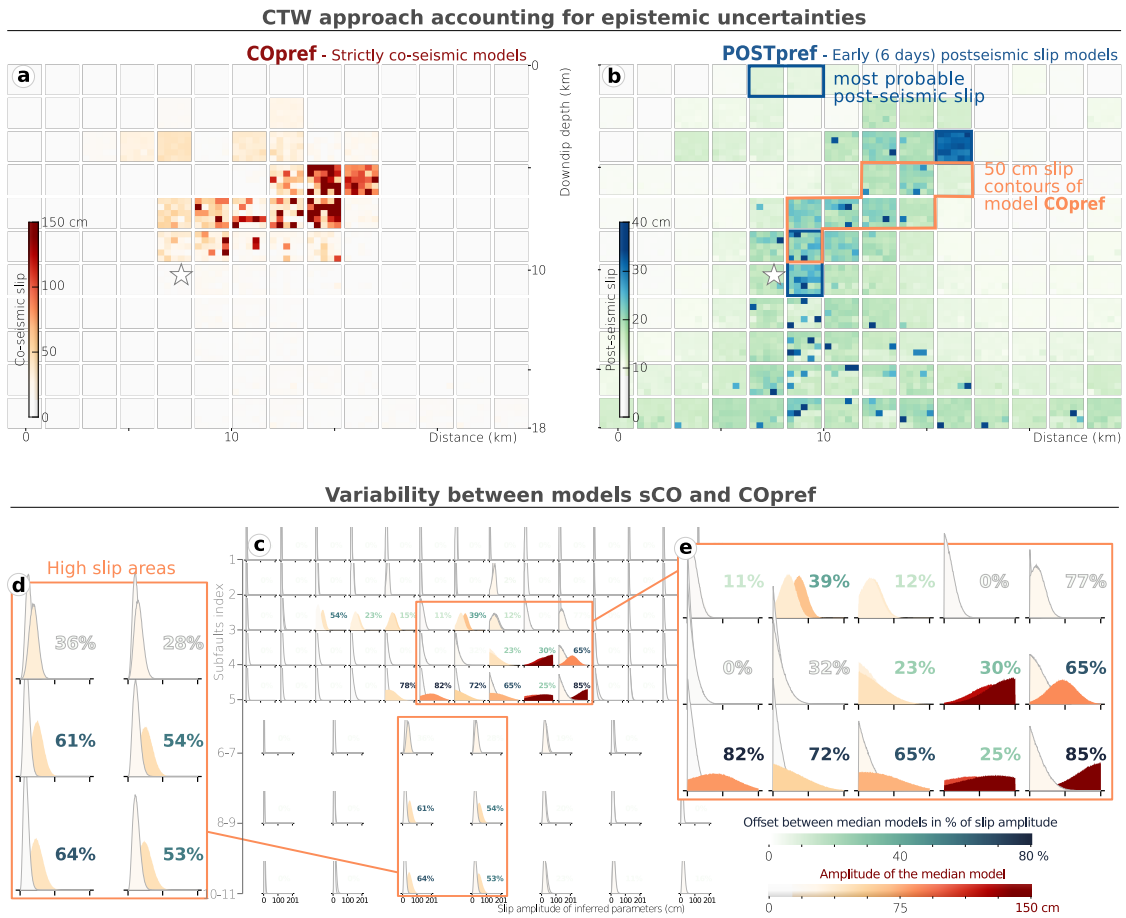


Figure 5. (a) and (b) Strictly co-seismic COpref and early postseismic POSTpref (6 days after the mainshock) preferred slip models (sum of strike- and dip-slip components), inferred with the CTW approach and accounting for epistemic uncertainties. (c) Comparison between the posterior Probability Density Functions of the dip-slip parameters of models COpref (a) and sCO (Figure 3c), colored from the amplitude of their median model. In the last four rows, the PDFs have been merged, covering 2 subfaults along strike and 2 subfaults along dip (i.e. patches two times bigger than for the first four rows). The COpref model PDFs are in the foreground while the sCO PDFs are in the background. The offset between the median models is shown as percentage with a different color scale. Two high slip areas are illustrated in detail: the highest slip patch (e) and the deep slip patch (d). The plots of the posterior PDFs are truncated between 0 and 200 cm to simplify the visualization.

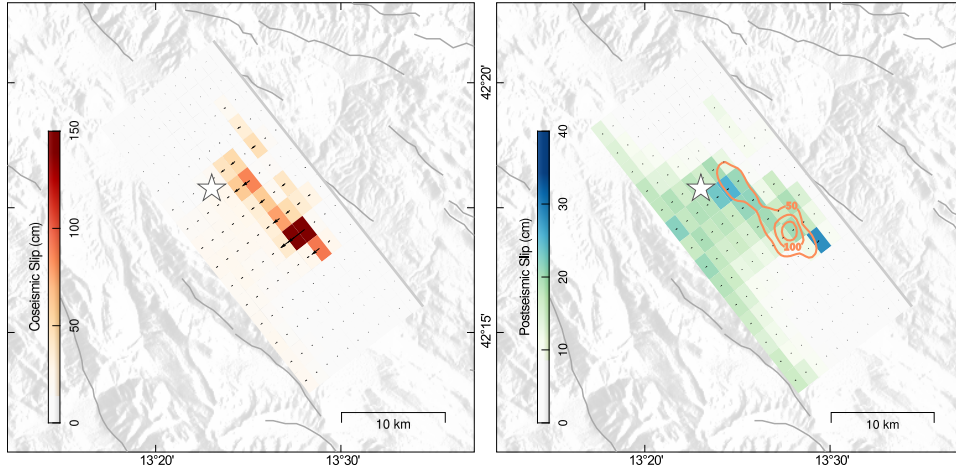


Figure 6. Our preferred slip models of the L'Aquila earthquake, inferred with the CTW approach and accounting for epistemic uncertainties. (a) and (b) show the dip-slip amplitude and rake of the average model in map view, the hypocenter being the white star. In (b), orange lines also show the 50 cm co-seismic slip contours.

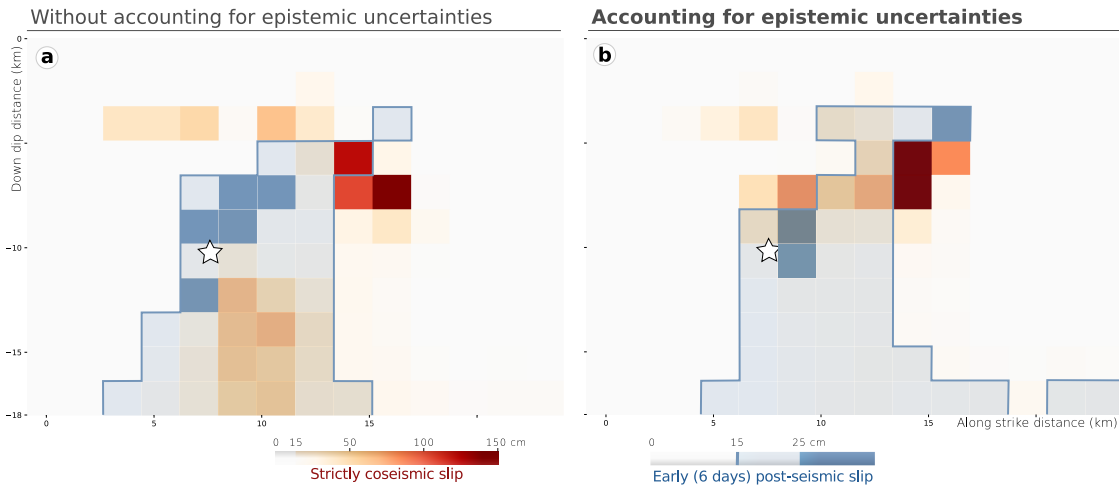


Figure 7. Effect of epistemic uncertainties (C_p) on the distribution of strictly co-seismic slip and afterslip. The slip models (sum of median strike- and dip-slip components) have been inferred accounting for epistemic uncertainties (b) or not (a). The strictly co-seismic slip median model is in light gray to dark orange colorscale. The subfaults that slipped of more than 15 and 25 cm up to 6 days after the mainshock, according to our median model, are in transparent light and medium blue respectively. The afterslip does not overlap the co-seismic slip when C_p is accounted for (b), whereas the two slip distributions overlap at depth when no C_p is included (a).

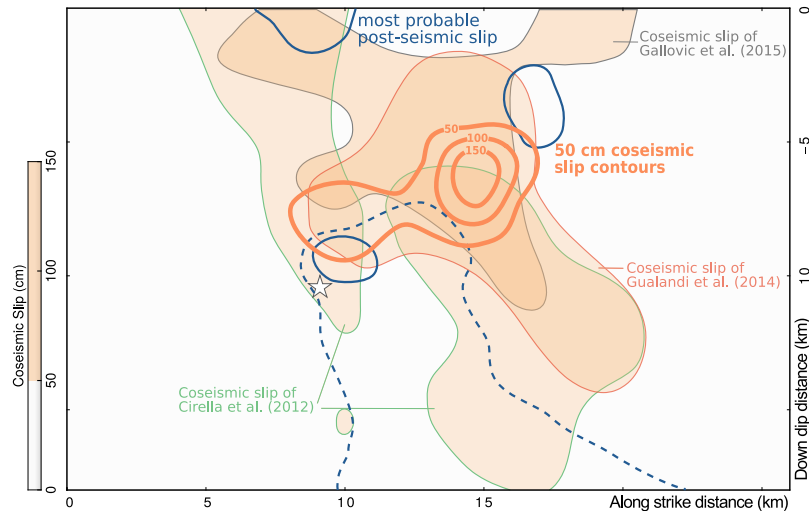


Figure 8. Comparison between the slip distributions inferred with the CTW approach and co-seismic slip distributions of other studies. The strictly co-seismic slip of *Gualandi et al.* [2014] inferred from GPS only, the strictly co-seismic slip of *Gallovic et al.* [2015] inferred from accelerometric and high rate GPS data, the co-seismic slip of *Cirella et al.* [2012] inferred from GPS, InSAR and strong motion, are projected in our fault plane in transparent light orange when slip exceeds 50 cm. The 50 cm contours of our strictly co-seismic slip distribution and the 15 cm contours of our afterslip inferred accounting for epistemic uncertainties are in bold lines, respectively orange and dark blue. The area of afterslip delimited with a dashed blue line is considered as less plausible as inferred with large uncertainties. The hypocenter is the white star.

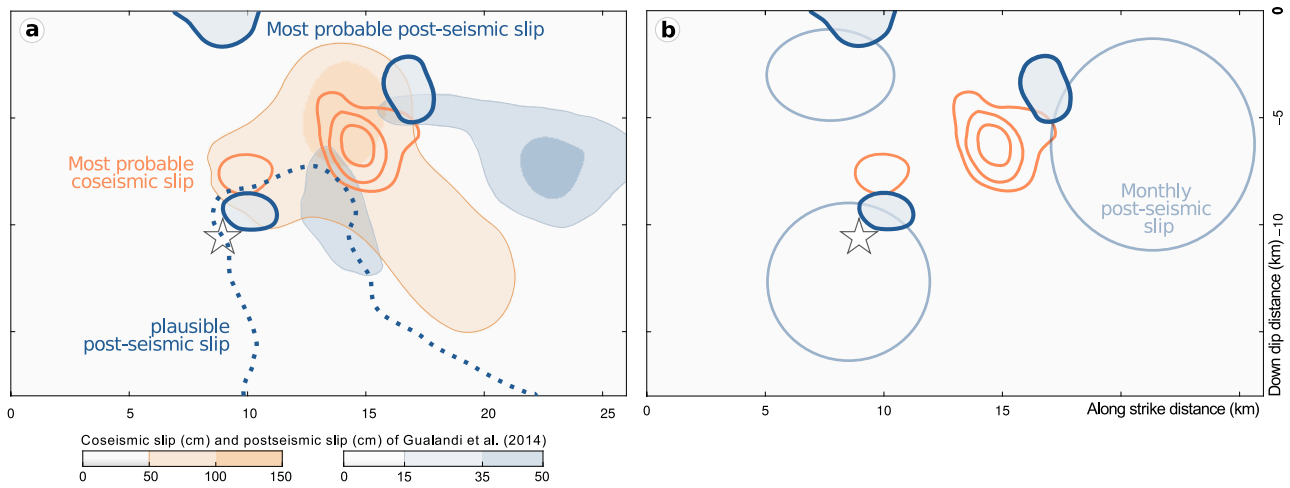


Figure 9. Comparison between our most probable strictly co- and post-seismic slip distribution 6 days after the mainshock and the post-seismic slip up to 306 days after the mainshock. (a) Our most probable slip distributions are represented with bold orange and dark blue lines, respectively for co-seismic (50 cm contours) and post-seismic slip (slip ≥ 10 cm). The area of afterslip delimited with a dotted blue line is considered as less plausible as inferred with large uncertainties. The co-seismic slip and afterslip 306 days after the mainshock inferred by *Gualandi et al.* [2014] are plotted with the same color codes but as color swaths. (b) Our results are compared to the area that slipped post-seismically during about 6 months (176 and 194 days respectively) after the mainshock as modeled by both *D’Agostino et al.* [2012] and *Cheloni et al.* [2014]. The hypocenter is the white star.

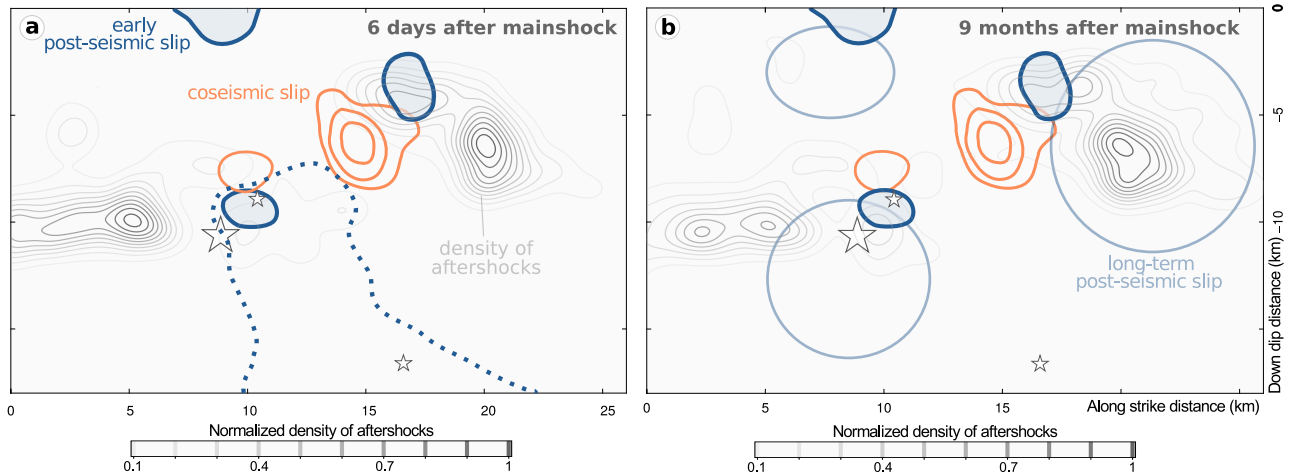


Figure 10. Distribution of most probable co-seismic slip and afterslip models, and the normalized density of aftershocks that occurred (a) within 6 days after the mainshock or (b) up to 9 months after the mainshock [$M_C = 0.88$, catalog of *Valoroso et al.*, 2013]. The strictly co-seismic 50 cm slip contours are in orange, while the contours of most probable afterslip (slip ≥ 10 cm) are in blue. The area delimited by dotted blue lines has plausibly hosted some afterslip, but not as probably as the other regions. The areas that slipped post-seismically during about 6 months after the mainshock as modeled by *D'Agostino et al.* [2012], *Cheloni et al.* [2014] and *Gualandi et al.* [2014] are the blue circles. The density of aftershocks located within 3 km of the fault (to account for potential uncertainty of the fault geometry) is calculated with a kernel density estimation method [*Parzen*, 1962] with a smoothing factor of 0.6. The cumulated number of aftershocks of $M_c = 0.88$ is of ~ 6000 6 days after the mainshock and 8 times larger 9 months after the mainshock (Figure S17). The hypocenter and aftershocks of $M_w \geq 4.4$ are the white stars.